

## Crustal radial anisotropy across Eastern Tibet and the Western Yangtze Craton

Jiayi Xie,<sup>1</sup> Michael H. Ritzwoller,<sup>1</sup> Weisen Shen,<sup>1</sup> Yingjie Yang,<sup>2</sup> Yong Zheng,<sup>3</sup> and Longquan Zhou<sup>4</sup>

Received 15 March 2013; revised 15 July 2013; accepted 16 July 2013; published 16 August 2013.

[1] Phase velocities across eastern Tibet and surrounding regions are mapped using Rayleigh (8–65 s) and Love (8–44 s) wave ambient noise tomography based on data from more than 400 Program for Array Seismic Studies of the Continental Lithosphere and Chinese Earthquake Array stations. A Bayesian Monte Carlo inversion method is applied to generate 3-D distributions of  $V_{sh}$  and  $V_{sv}$  in the crust and uppermost mantle from which radial anisotropy and isotropic  $V_s$  are estimated. Each distribution is summarized with a mean and standard deviation, but is also used to identify “highly probable” structural attributes, which include (1) positive midcrustal radial anisotropy ( $V_{sh} > V_{sv}$ ) across eastern Tibet (spatial average =  $4.8\% \pm 1.4\%$ ) that terminates abruptly near the border of the high plateau, (2) weaker ( $-1.0\% \pm 1.4\%$ ) negative radial anisotropy ( $V_{sh} < V_{sv}$ ) in the shallow crust mostly in the Songpan-Ganzi terrane, (3) negative midcrustal anisotropy ( $-2.8\% \pm 0.9\%$ ) in the Longmenshan region, (4) positive midcrustal radial anisotropy ( $5.4\% \pm 1.4\%$ ) beneath the Sichuan Basin, and (5) low  $V_s$  in the middle crust ( $3.427 \pm 0.050$  km/s) of eastern Tibet. Midcrustal  $V_s < 3.4$  km/s (perhaps consistent with partial melt) is highly probable only for three distinct regions: the northern Songpan-Ganzi, the northern Chuandian, and part of the Qiangtang terranes. Midcrustal anisotropy provides evidence for sheet silicates (micas) aligned by deformation with a shallowly dipping foliation plane beneath Tibet and the Sichuan Basin and a steeply dipping or subvertical foliation plane in the Longmenshan region. Near vertical cracks or faults are believed to cause the negative anisotropy in the shallow crust underlying Tibet.

**Citation:** Xie, J., M. H. Ritzwoller, W. Shen, Y. Yang, Y. Zheng, and L. Zhou (2013), Crustal radial anisotropy across Eastern Tibet and the Western Yangtze Craton, *J. Geophys. Res. Solid Earth*, 118, 4226–4252, doi:10.1002/jgrb.50296.

### 1. Introduction

[2] The amplitude and distribution of elastic anisotropy in Earth’s crust and mantle provide valuable information about the deformation history of the solid earth. Mantle anisotropy has been particularly well studied in the laboratory and in the field and is believed principally to reflect the lattice preferred orientation of olivine produced by mantle kinematics [e.g., Schlue and Knopoff, 1977; Montagner and Anderson, 1989; Montagner and Tanimoto, 1991; Ekström and Dziewonski, 1998; Mainprice, 2007; Becker et al., 2008]. Crustal anisotropy has probably been explored less fully although seismological studies that relate observed anisotropy to crustal deformation and metamorphism have been developing rapidly

[e.g., Okaya et al., 1995; Levin and Park, 1997; Godfrey et al., 2000; Vergne et al., 2003; Ozacar and Zandt, 2004; Shapiro et al., 2004; Sherrington et al., 2004; Champion et al., 2006; Xu et al., 2007a, 2007b; Readman et al., 2009]. In parallel, petrophysical understanding of the causes of crustal anisotropy has also been growing quickly [e.g., Barruol and Mainprice, 1993; Nishizawa and Yoshino, 2001; Okaya and McEvilly, 2003; Cholach et al., 2005; Cholach and Schmitt, 2006; Kitamura, 2006; Mahan, 2006; Barberini et al., 2007; Tatham et al., 2008; Lloyd et al., 2009; Ward et al., 2012; M. B. Erdman et al., Seismic anisotropy of the crust: Electron backscatter diffraction measurements from the Basin and Range, accepted to *Geophysical Journal International*, 2013]. With the development of ambient noise tomography, surface waves now can be observed at periods short enough to allow shear wave speed models to be constructed at crustal depths including models both of azimuthal [e.g., Lin et al., 2011; Xie et al., 2012] and polarization or radial [e.g., Bensen et al., 2009; Huang et al., 2010; Moschetti et al., 2010a, 2010b; Takeo et al., 2013] anisotropy. The current paper reports on the application of ambient noise tomography to infer radial anisotropy in eastern Tibet and surrounding regions.

[3] Radial anisotropy is a property of a medium in which the speed of the wave depends on its polarization and direction of

<sup>1</sup>Center for Imaging the Earth’s Interior, Department of Physics, University of Colorado Boulder, Boulder, Colorado, USA.

<sup>2</sup>Department of Earth and Planetary Sciences, Macquarie University, Sydney, New South Wales, Australia.

<sup>3</sup>State Key Laboratory of Geodesy and Earth’s Dynamics, Institute of Geodesy and Geophysics, Chinese Academy of Sciences, Wuhan, China.

<sup>4</sup>China Earthquake Network Center, Beijing, China.

Corresponding author: J. Xie, Center for Imaging the Earth’s Interior, Department of Physics, University of Colorado Boulder, Campus Box 390, Boulder, CO 80309, USA. (jiayi.xie@colorado.edu)

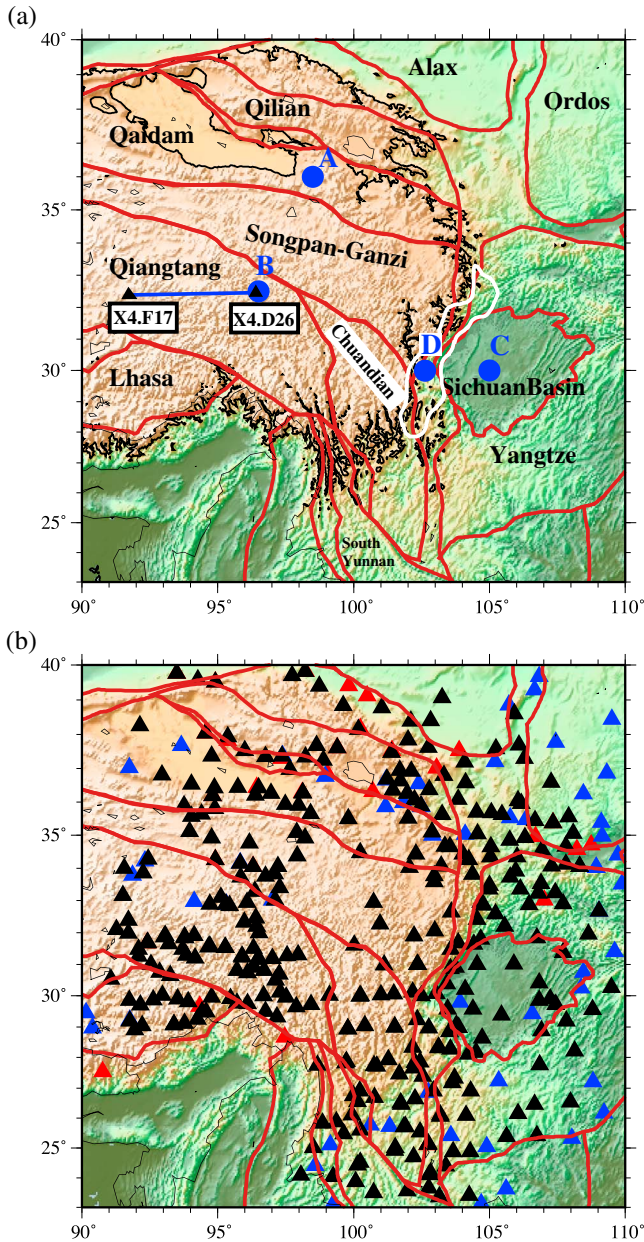


**Figure 1.** (a) Reference map of the study region in which red lines indicate the boundaries of major geological units and basins [Zhang et al., 1984, 2003]. The white contour outlines what we refer to as the Longmenshan region. The blue line is the path between stations X4.F17 and X4.D26 referenced in Figure 2. Points A, B, C, and D indicate sample points referenced in Figures 6, 7, 13, 16, 17, and 19. (b) Locations of seismic stations used in this study. Red and black triangles are stations used to measure Love wave dispersion, while blue and black triangles indicate stations used for Rayleigh wave measurements.

propagation. For a transversely isotropic medium, such as a medium with hexagonal symmetry with a vertical symmetry axis, there are two shear wave speeds:  $V_{sv}$  and  $V_{sh}$ . In such a medium, a shear wave that is propagating horizontally and polarized vertically or a shear wave that is propagating vertically and polarized horizontally will propagate with speed  $V_{sv}$ . In contrast, a wave that is propagating in a horizontal

direction and polarized horizontally will propagate with speed  $V_{sh}$ . We refer to this difference in wave speed as  $V_s$  radial anisotropy or in some places merely as radial anisotropy, which is represented here as the percentage difference between  $V_{sh}$  and  $V_{sv}$  in the medium:  $\gamma = (V_{sh} - V_{sv})/V_s$ . In this case,  $V_s$  is the isotropic or effective shear wave speed and is computed from  $V_{sh}$  and  $V_{sv}$  via a Voigt average,  $V_s = \sqrt{(2V_{sv}^2 + V_{sh}^2)}/3$  [Babuška and Cara, 1991].

[4] The direct observation of radial anisotropy with regionally propagating shear waves, which are confined to the crust and uppermost mantle, is extremely difficult. Thus, the existence of radial anisotropy is typically inferred from observations of a period-dependent discrepancy between the phase or group speeds of Rayleigh and Love waves. As discussed later in the paper and in many other papers [e.g., Anderson and Dziewonski, 1982; Montagner and Nataf, 1986], Rayleigh waves are strongly sensitive to  $V_{sv}$  and Love waves to  $V_{sh}$ . The Rayleigh-Love discrepancy is identified by the inability of a simply parameterized isotropic shear velocity model to fit the dispersion characteristics of both types of waves simultaneously. Observations of this discrepancy attributed to radial anisotropy in the mantle in which  $V_{sh} > V_{sv}$  date back about half a century [Aki, 1964; Aki and Kaminuma, 1963; McEvelly, 1964; Takeuchi et al., 1968]. Much more recently, radial anisotropy in the uppermost mantle has been mapped worldwide [Montagner and Tanimoto, 1991; Trampert and Woodhouse, 1995; Babuška et al., 1998; Ekström and Dziewonski, 1998; Shapiro and Ritzwoller, 2002; Nettles and Dziewoński, 2008], and there have also been inroads made into mapping radial anisotropy in the crust beneath the U.S. [Bensen et al., 2009; Moschetti et al., 2010a, 2010b] and Tibet [Shapiro et al., 2004; Chen et al., 2010; Duret et al., 2010; Huang et al., 2010]. The observations in Tibet are part of a steady improvement in the reliability and the lateral and radial resolutions of surface wave dispersion studies that cover all [Ritzwoller et al., 1998; Villaseñor et al., 2001; Levshin et al., 2005; Maceira et al., 2005; Zheng et al., 2008; Caldwell et al., 2009; Acton et al., 2010; Yang et al., 2010, 2012] or parts of the high plateau [Levshin et al., 1994; Cotte et al., 1999; Rapine et al., 2003; Yao et al., 2008, 2010; Guo et al., 2009; Li et al., 2009; Jiang et al., 2011; Zhou et al., 2012].

[5] The observation of crustal radial anisotropy has been taken as evidence for the existence of strong elastically anisotropic crustal minerals aligned by strains associated with processes of deformation [Shapiro et al., 2004; Moschetti et al., 2010a, 2010b]. Many continental crustal minerals are strongly anisotropic as single crystals [Barruol and Mainprice, 1993; Mahan, 2006], but some of the most common minerals (e.g., feldspars and quartz) have geometrically complicated anisotropic patterns that destructively interfere with polycrystalline aggregates [Lloyd et al., 2009; Ward et al., 2012]. Micas and amphiboles are exceptions that exhibit more robust alignment in both crystallographic direction and shape that produce simple patterns of seismic anisotropy [Tatham et al., 2008; Lloyd et al., 2009]. For this reason, recent observations of strong anisotropy in the middle crust have been attributed to the crystallographic preferred orientation (CPO) of mica [Nishizawa and Yoshino, 2001; Shapiro et al., 2004; Moschetti et al.,

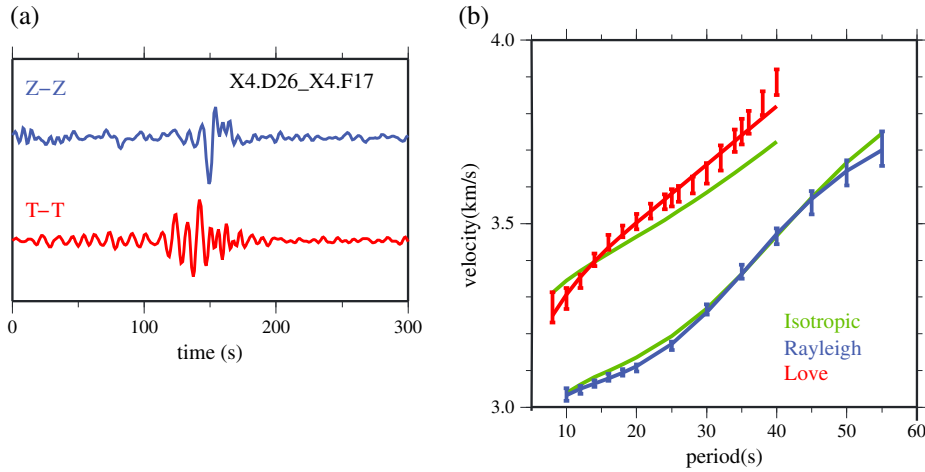


**Figure 2.** (a) Example of Rayleigh wave (blue, vertical-vertical, Z-Z) and Love wave (red, transverse-transverse, T-T) cross correlations for a pair of stations (X4.F17, X4.D26) located in the Qiangtang terrane (Figure 1a), band pass filtered between 5 and 100 s period. (b) Observed Rayleigh and Love wave phase speed curves measured from the cross correlations are presented as 1 standard deviation ( $1\sigma$ ) error bars (red-Love, blue-Rayleigh). Inverting these data for an isotropic model ( $V_s = V_{sh} = V_{sv}$ ) produces the best-fitting green curves, which demonstrates a systematic misfit to the data (predominantly the Love waves) and a Rayleigh-Love discrepancy. Allowing crustal anisotropy ( $V_{sh} \neq V_{sv}$ ) produces the blue and red dispersion curves that fit the data.

2010a, 2010b]. In the lower crust, amphibole may also be an important contributor to seismic anisotropy [Kitamura, 2006; Barberini *et al.*, 2007; Tatham *et al.*, 2008].

[6] Shapiro *et al.* [2004] showed that crustal radial anisotropy is strong in western Tibet and may extend into eastern Tibet where the resolution of their study was weaker. Subsequently, Duret *et al.* [2010] presented evidence from individual seismograms using aftershocks of the Wenchuan earthquake of 12 May 2008 that the Rayleigh-Love discrepancy is so significant for paths crossing Tibet that crustal radial anisotropy probably also extends into eastern Tibet. Huang *et al.* [2010] confirmed this expectation by mapping crustal radial anisotropy in far southeastern Tibet. Example cross correlations of ambient noise for a path in the Qiangtang terrane (Figure 1) contain Rayleigh and Love waves as shown in Figure 2a. Figure 2b illustrates that a Rayleigh-Love discrepancy exists for this path, revealing that crustal radial anisotropy, indeed, is present between stations located within eastern Tibet.

[7] The objective of this paper is to map crustal radial anisotropy across all of eastern Tibet (Figure 1), extending the results into adjacent areas north and east of the high plateau for comparison. Rayleigh and Love wave phase velocity curves are measured from ambient noise cross correlations between each pair of simultaneously operating stations between 8 and 44 s period for Love waves and 8 and 65 s for Rayleigh waves. As shown later, the inability to observe Love waves at longer periods implies that radial anisotropy cannot be reliably mapped deeper than about 50 km, which means that we cannot place tight constraints on the strength of radial anisotropy in the lowermost crust beneath Tibet. For this reason, we focus discussion on midcrustal radial anisotropy.

[8] The inversion of surface wave data for a 3-D radially anisotropic shear wave speed model consists of two stages: first, a tomographic inversion is performed using measured Rayleigh and Love wave dispersion curves for period-dependent phase speed maps on a  $0.5^\circ \times 0.5^\circ$  grid using the tomographic method

of Barmin *et al.* [2001] with uncertainties estimated using eikonal tomography [Lin *et al.*, 2009] (section 2), and second, a Bayesian Monte Carlo inversion [Shen *et al.*, 2013b] is carried out for a 3-D radially anisotropic shear velocity ( $V_{sv}$  and  $V_{sh}$ ) model of the crust (section 3). The inversion estimates the posterior distribution of accepted models at each location, which is used in two ways. First, at each grid node, we summarize the distribution at each depth with its mean and standard deviation. Using the mean of the distribution, we show that strong midcrustal positive ( $V_{sh} > V_{sv}$ ) radial anisotropy is observed across all of eastern Tibet and terminates abruptly as the border of the high plateau is reached. It is also observed in the middle crust beneath the Sichuan Basin. Negative radial anisotropy ( $V_{sv} > V_{sh}$ ) is observed in the shallow crust beneath eastern Tibet and in the middle crust of the Longmenshan region. Second, we also query the entire posterior distribution of models in order to determine which structural attributes are highly probable, which are only likely, and which are prohibited. Throughout, we attempt to address how uncertainties in prior knowledge (e.g.,  $V_p/V_s$  in the crust) affect the key inferences. In particular, we investigate if prior constraints and assumptions are likely to bias the posterior distribution significantly. Finally, we ask how the observations reflect on the presence or absence of pervasive partial melt in the middle crust across Tibet and speculate on the physical causes of several observed radial anisotropy features.

## 2. Data Processing and Tomography

### 2.1. Love Wave and Rayleigh Wave Tomography

[9] For Love wave data processing, we apply the procedure described by Bensen *et al.* [2007] and Lin *et al.* [2008] to recordings at 362 stations (Figure 1), consisting of 180 Program for Array Seismic Studies of the Continental Lithosphere (PASSCAL) and Global Seismic Network (GSN) stations and 182 Chinese Earthquake Array (CEArray) stations [Zheng

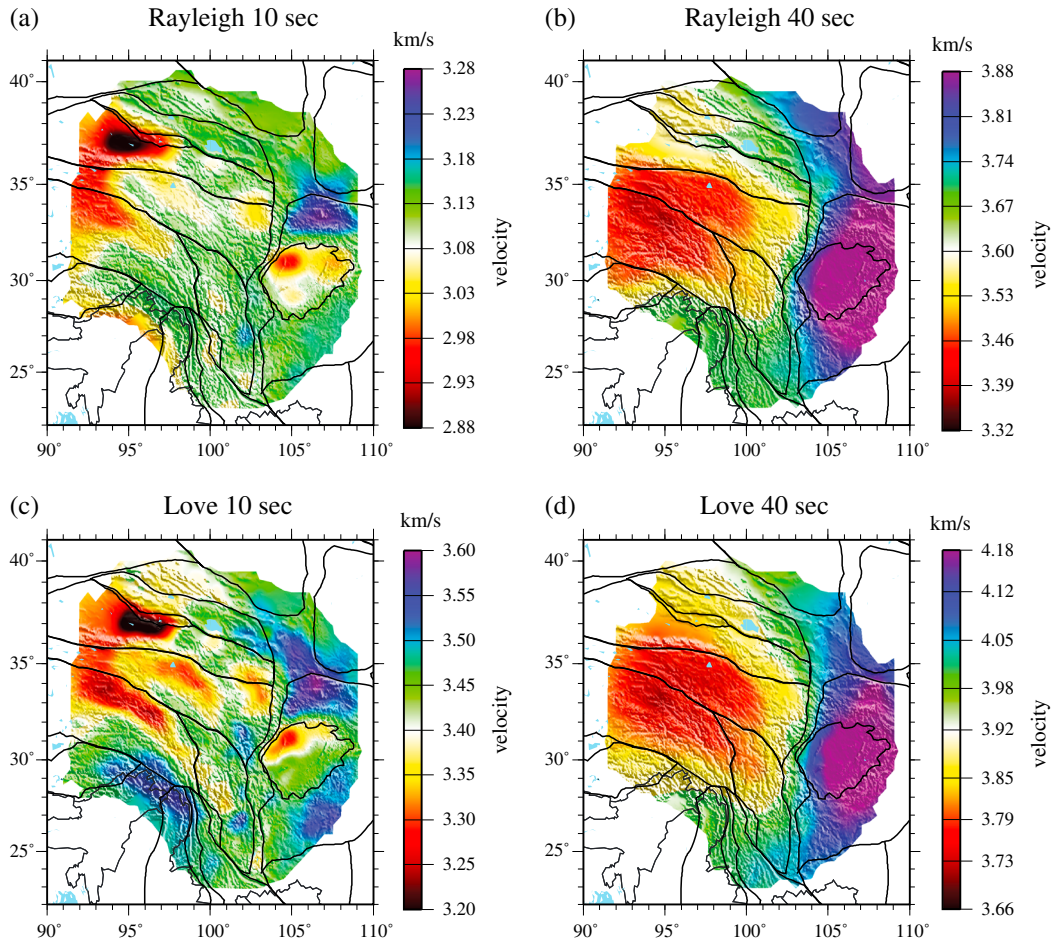


**Figure 3.** Example of estimated (a and b) Rayleigh and (c and d) Love wave phase speed maps at 10 (Figures 3a and 3c) and 40 s (Figures 3b and 3d) period determined from ambient noise cross correlations.

*et al.*, 2010]. We downloaded all available horizontal component data for PASSCAL and GSN stations between years 2000 and 2011 from the Incorporated Research Institutions for Seismology Data Management Center. Horizontal component data for the CEArray stations were acquired for the years 2007 through 2009. We cut horizontal component ambient noise records into 1-day long time series and then cross-correlate the transverse components (T-T) between all possible station pairs, after the performance of the time domain and frequency domain normalization procedures described by *Bensen et al.* [2007]. As *Lin et al.* [2008] demonstrated, Love wave energy dominates transverse-transverse (T-T) cross correlations. *Yang and Ritzwoller* [2008] showed that Rayleigh wave cross correlations between stations in Tibet are typically not symmetric, but there is significant energy from most directions with the primary directions of propagation of the waves being dependent on both period and season. This is also true for Love waves, but the strongest waves (highest signal-to-noise ratio (SNR)) typically come from the southeast. After the cross correlations, we applied automated frequency-time analysis (FTAN) [e.g., *Levshin and Ritzwoller*, 2001; *Bensen et al.*, 2007] to produce Love wave phase speed curves for periods between 8 and 30 to 50 s (depending on the signal-to-noise ratio) for each station pair.

[10] Rayleigh wave phase speed measurements are obtained from cross correlations of vertical-component ambient noise,

the vertical-vertical (Z-Z) cross correlations, which are rich in Rayleigh waves. *Yang et al.* [2010] generated Rayleigh wave phase velocity maps from ambient noise across the Tibetan Plateau. Instead of using their dispersion maps directly, we reselected the measurements for stations within our study region and reperformed the tomography as described below. Example T-T and Z-Z cross correlations and measured phase speeds between the station pair X4.D26 and X4.F17 are shown in Figure 2.

[11] For dispersion measurements at different periods, we exploited three criteria to identify reliable measurements: (1) the distance between two stations must be greater than two wavelengths to ensure sufficient separation of the surface wave packet from precursory arrivals and noise and to satisfy the far-field approximation (the use of a three-wavelength criterion changes results negligibly); (2) measurements must have a signal-to-noise ratio (SNR)  $> 10$  for Love wave and  $> 15$  for Rayleigh wave to ensure the reliability of the signal; and (3) the observed travel times and those predicted from the associated phase velocity map between each accepted station pair must agree within a specified tolerance [*Zhou et al.*, 2012]. We found that horizontal components are problematic (mainly relative to criterion (3) above) for 61 stations. Their removal left us with the 362 stations shown in Figure 1. The vertical components of 26 stations are similarly identified as problematic and are rejected from further

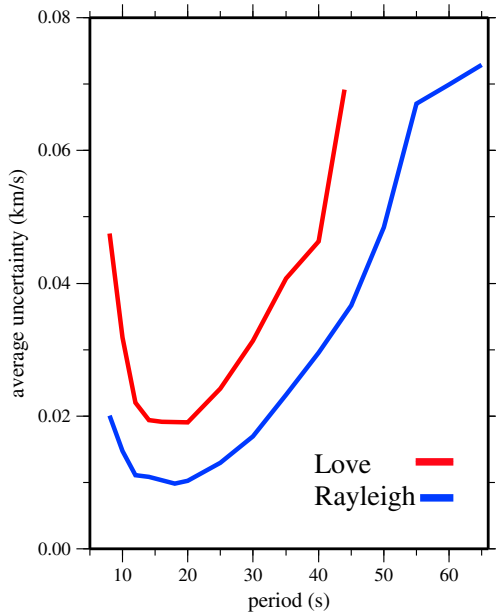


**Figure 4.** Uncertainties ( $1\sigma$ ) in the Rayleigh and Love wave phase speed maps averaged across the study region estimated using the eikonal tomography method of *Lin et al.* [2009].

analysis leaving 406 stations from which we obtain Rayleigh wave measurements. This procedure produces about 30,000 Love wave phase velocity curves and 40,000 Rayleigh wave curves.

[12] Because eikonal tomography [*Lin et al.*, 2009] models off-great circle propagation, it would be preferable to straight-ray tomography [*Barmin et al.*, 2001]. Eikonal tomography works best, however, where there are no spatial gaps in the array of stations. There are gaps in our station coverage near  $33^\circ\text{N}$ ,  $100^\circ\text{E}$  in eastern Tibet (Figure 1b). Thus, we apply straight-ray tomography [*Barmin et al.*, 2001] to generate phase velocity maps, but use eikonal tomography to estimate uncertainties in these maps, as described in section 2.2. To reduce the effect of nonideal azimuthal coverage at some locations, we simultaneously estimate azimuthal anisotropy, but these estimates are not used here. What results are Love wave phase velocity maps ranging from 8 to 44 s and Rayleigh wave phase velocity maps from 8 to 65 s period. Above 44 s period, the SNR of Love waves decreases dramatically, which degrades the ability to produce reliable high-resolution maps. Examples of Rayleigh and Love wave phase speed maps at periods of 10 and 40 s are shown in Figure 3. At 10 s period, the maps are quite sensitive to shallow crustal structures to about 20 km depth including the existence of sediments, and at 40 s period, the maps are predominantly sensitive to structures near the Moho such as crustal thickness.

## 2.2. Uncertainties and Local Dispersion Curves

[13] Local uncertainty estimates for each of the phase speed maps provide the uncertainties used in the inversion for 3-D structure. Estimates of uncertainties in the Rayleigh and Love wave phase speed maps are determined by eikonal tomography [*Lin et al.*, 2009], which, as discussed above, does not produce uniformly unbiased phase speed estimates

where there are gaps in station coverage. We find, however, that it does produce reliable uncertainty estimates, even in the presence of spatial gaps. Averaging the one-standard deviation uncertainty maps across the study region, average uncertainties are found to range between 0.012 to 0.057 km/s for Rayleigh waves and 0.016 to 0.060 km/s for Love waves (Figure 4), minimize between about 12 and 25 s period, and increase at both shorter and longer periods. Because of the lower SNR and the smaller number of Love wave measurements, uncertainties for Love waves tend to be larger than for Rayleigh waves. In addition, the SNR decreases faster at long periods for Love waves than Rayleigh waves, so the uncertainty for Love waves at long periods is higher still than for Rayleigh waves. Uncertainties for both wave types increase toward the borders of the maps at all periods.

[14] Having estimated maps of period-dependent dispersion and uncertainty, local Rayleigh and Love wave dispersion curves with associated uncertainties are generated on a  $0.5^\circ \times 0.5^\circ$  grid across the study region. These data are the input for the 3-D model inversion that follows.

## 3. Bayesian Monte Carlo Inversion of Local Dispersion Curves

### 3.1. Model Parameterization and Prior Constraints

[15] The 3-D model comprises a set of 1-D models situated on a  $0.5^\circ \times 0.5^\circ$  grid. Following *Shen et al.* [2013a, 2013b],

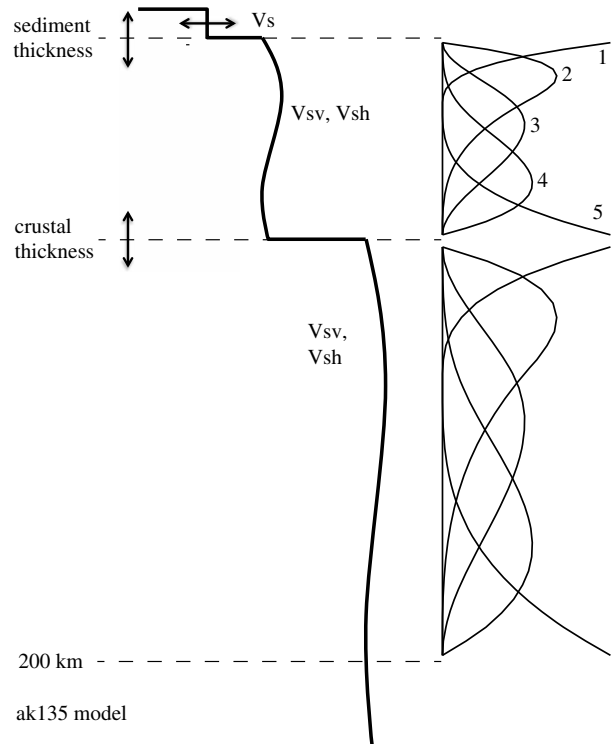


**Figure 5.** Representation of the parameterization used across the study region. In the crust, five B-splines (1–5) are used to represent  $V_{sv}$ , but three B-splines (2–4) are used to represent  $V_{sh}$ . In the mantle, five B-splines are estimated for  $V_{sv}$  but  $V_{sh}$  is derived from the strength of radial anisotropy in the model of *Shapiro and Ritzwoller* [2002]. A total of 16 parameters represent the model at each spatial location.

**Table 1.** Model Parameter Constraints

	Model Parameter	Perturbation	Reference Model
Sedimentary layer	Sediment thickness	$\pm 100\%$	<i>Laske and Masters [1997]</i>
	Vsv in sediment	$\pm 1.0$ km/s	
	Vsh in sediment	Equals to Vsv	
Crystalline crustal layer	Crustal thickness	$\pm 10\%$	<i>Shapiro and Ritzwoller [2002]</i>
	Five Vsv B-splines <sup>a</sup>	$\pm 20\%$	
	Five Vsh B-splines <sup>a</sup>	$\pm 20\%$	
Mantle layer to 150 km	Five Vsv B-splines	$\pm 20\%$	<i>Shapiro and Ritzwoller [2002]</i>
	Anisotropy	0	

$$^a \Delta v / \Delta h \geq 0 \text{ or } -1/70 \text{ s}^{-1} \leq \Delta v / \Delta h < 0.$$

each of the 1-D models is parameterized with three principal layers: a sedimentary layer, a crystalline crustal layer, and a mantle layer to a depth of 200 km. The sedimentary layer is isotropic and is described by two parameters: layer thickness and constant shear wave speed  $V_s$ . Anisotropy in the sedimentary layer is physically possible, but with the data used here cannot be resolved from anisotropy in the crystalline crust. In addition, it has little effect in the period range of the observed Rayleigh-Love discrepancy as discussed further in section 4. For these reasons, we include anisotropy only below the sediments.

[16] We represent anisotropy through the elastic moduli of a transversely anisotropic medium (also referred to as radial anisotropy). In such a medium, the elastic tensor is specified by five moduli:  $A$ ,  $C$ ,  $L$ ,  $N$ , and  $F$ . The moduli  $A$  and  $C$  are related to the  $P$  wave speeds ( $V_{ph}$  and  $V_{pv}$ ), and  $L$  and  $N$  are related to the  $S$  wave speeds ( $V_{sv}$  and  $V_{sh}$ ) as follows:  $A = \rho V_{ph}^2$ ,  $C = \rho V_{pv}^2$ ,  $L = \rho V_{sv}^2$ , and  $N = \rho V_{sh}^2$ , where  $\rho$  is density. Some authors summarize radial anisotropy with three derived parameters:  $\xi = N/L = (V_{sh}/V_{sv})^2$ ,  $\phi = C/A = (V_{pv}/V_{ph})^2$ , and  $\eta = F/(A - 2L)$ . We prefer to summarize  $V_s$  and  $V_p$  anisotropy with two different parameters in addition to  $\eta$ , defined as follows:  $\gamma = (V_{sh} - V_{sv})/V_s$  and  $\varepsilon = (V_{ph} - V_{pv})/V_p$ , where  $V_s$  is the Voigt average of  $V_{sh}$  and  $V_{sv}$ , and  $V_p$  similarly is the Voigt average of  $V_{ph}$  and  $V_{pv}$ . We refer to  $\gamma$  as  $V_s$  radial anisotropy and  $\varepsilon$  as  $V_p$  radial anisotropy. These parameters are simply related to those used by some other authors:  $\gamma + 1 \approx \xi^{1/2}$  and  $\varepsilon + 1 \approx \phi^{-1/2}$ . In an isotropic medium,  $V_{sh} = V_{sv}$ ,  $V_{ph} = V_{pv}$ , and  $F = A - 2L$ , thus  $\xi = \phi = \eta = 1$  and  $\gamma = \varepsilon = 0$ .

[17] We make the simplifying (but nonphysical) assumption that only  $V_s$  anisotropy is present in the elastic tensor in the crust and mantle. Thus, we allow  $V_{sh}$  to differ from  $V_{sv}$ , but restrict  $V_{ph} = V_{pv}$  ( $\varepsilon = 0$ ) and  $\eta = 1$ . Strictly speaking, this is physically unrealistic because in real mineral assemblages,  $V_s$  anisotropy would be accompanied by  $V_p$  anisotropy with  $\eta$  differing from unity [e.g., *Babuška and Cara, 1991; Erdman et al., 2013*]. In section 5.4.4, we show, however, that the effect of this assumption on our estimate of crustal  $V_s$  anisotropy is negligible. Therefore, although we represent radial anisotropy in terms of  $V_s$  anisotropy alone, our results are consistent with the inclusion of  $V_p$  anisotropy in the elastic tensor along with  $\eta$  that differs from unity.

[18] The crystalline crustal layer is described by nine parameters: layer thickness, five B-splines (1–5) for  $V_{sv}$  (Figure 5), and three more independent B-splines for  $V_{sh}$  (2–4). We set  $V_{sh} = V_{sv}$  for B-splines 1 and 5. Because B-splines 2 and 4 extend into the uppermost

and lowermost crust, respectively, radial anisotropy can extend into these regions but its amplitude will be reduced relative to models in which  $V_{sh}$  and  $V_{sv}$  for B-splines 1 and 5 are free. The effect of this constraint is discussed in section 5.4.1.

[19] Mantle structure is modeled from the Moho to 200 km depth with five B-splines for  $V_{sv}$ .  $V_{sh}$  in the mantle differs from  $V_{sv}$  by the depth-dependent strength of radial anisotropy taken from the 3-D model of *Shapiro and Ritzwoller [2002]*. Thus, in the mantle, we estimate  $V_{sv}$ , but set  $V_{sh} = V_{sv} + \delta V$  where  $\delta V$  is the difference between  $V_{sh}$  and  $V_{sv}$  in the model of *Shapiro and Ritzwoller [2002]*. Below 200 km, the model reverts to the 1-D model ak135 [*Kennett et al., 1995*]. The effect on estimates of crustal anisotropy caused by fixing the amplitude of mantle anisotropy is considered in section 5.4.2. Overall, there are 16 free parameters at each point and the model parameterization is uniform across the study region.

[20] Because Rayleigh and Love wave velocities are mainly sensitive to shear wave speeds, other variables in the model such as compressional wave speed,  $V_p$ , and density,  $\rho$ , are scaled to the isotropic shear wave speed model,  $V_s$ .  $V_p$  is converted from  $V_s$  using a  $V_p$  to  $V_s$  ratio such that  $V_p/V_s$  is 2.0 in the sediments and 1.75 in the crystalline crust and mantle, consistent with a Poisson solid. For density, we use a scaling relation that has been influenced by the studies of *Christensen and Mooney [1995]* and *Brocher [2005]* in the crust and by *Karato [1993]* in the mantle, where sensitivity to density structure is much weaker than in the crust. The Q model comes from ak135 [*Kennett et al., 1995*] with some modifications: shear Q is 600 in the upper 20 km and 400 between 20 and 80 km depth outside the Tibetan Plateau, while we set it to 250 within the Tibetan Plateau [*Levshin et al., 2010*].  $V_s$ ,  $V_{sv}$ , and  $V_{sh}$  are converted to a reference period of 1 s. To test the effect of uncertainties in the physical dispersion correction [*Kanamori and Anderson, 1977*] on estimates of  $V_{sv}$  and  $V_{sv}$  caused by ignorance of the Q of the crust, we lowered values of Q from 250 to 100 between 20 and 80 km depth. We found that the amplitude of the resulting depth-averaged crustal radial anisotropy decreased only slightly for the smaller Q beneath point B shown in Figure 1a. As a constant Q of 100 between these depths is almost certainly too low, and we are concerned with anisotropy amplitudes greater than 1%, uncertainties in the Q model can be ignored here.

[21] To avoid consideration of physically unreasonable models, we imposed prior constraints on the parameter space explored in the inversion. (1) Although velocity is not constrained to increase monotonically with depth, it cannot decrease with depth at a rate ( $-\Delta v/h\Delta$ ) larger than  $1/70 \text{ s}^{-1}$ . This constraint reduces (but does not entirely eliminate) the tendency of the shear wave speeds to oscillate with depth. (2) Shear wave speeds increase with depth across the sediment-basement interface and across Moho. (3) Both  $V_{sv}$  and  $V_{sh}$  are constrained to be less than 4.9 km/s at all depths. (4) The amplitude of radial anisotropy in the uppermost and lowermost crust is constrained by setting  $V_{sh} = V_{sv}$  for splines 1 and 5 (Figure 5). The last constraint is imposed to mitigate against radial anisotropy oscillating with depth, and its effect is discussed further in section 5.4.1.

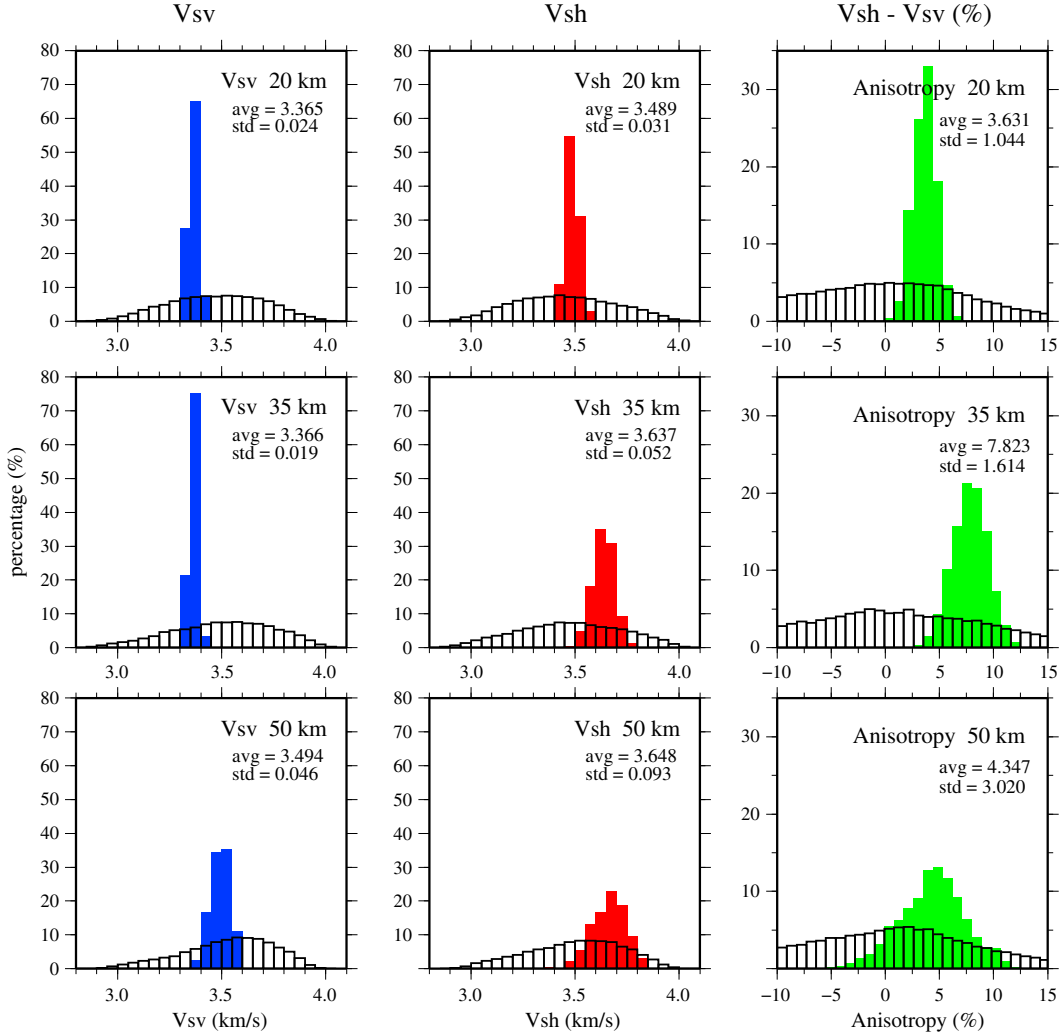


**Figure 6.** Prior (white histograms) and posterior distributions for Vsv (blue), Vsh (red), and Vs radial anisotropy (green,  $\gamma$  in percent) at 20, 35, and 50 km depth for point B in the Qiangtang terrane (Figure 1a). The mean and standard deviation for each posterior distribution are shown in each panel.

[22] The model space is then explored starting with perturbations (Table 1) to a reference model consisting of sedimentary structure from *Laske and Masters* [1997] and crystalline crustal and uppermost mantle structure from *Shapiro and Ritzwoller* [2002]. Imposing the prior constraints in model space defines the prior distribution of models, which aims to quantify the state of knowledge before data are introduced. In particular, a new model  $m_i$  is generated by perturbing the initial model  $m_0$  following the procedure described by *Shen et al.* [2013b]. The set of all models that can be produced in this way is called the prior distribution, and example plots for various model variables are shown in Figure 6.

### 3.2. Inversion Procedure

[23] With the parameterization and constraints described above, we perform a Bayesian Monte Carlo inversion based on the method described by *Shen et al.* [2013b]. This method is modified to produce a radially anisotropic model using both Love and Rayleigh wave data without receiver functions. The main modifications lie in the forward calculation of surface wave dispersion for a transversely isotropic (radially anisotropic) medium, which we base on the code MINEOS

[*Masters et al.*, 2007]. Unlike most seismic dispersion codes, the MINEOS code consistently models a transversely isotropic medium. In order to accelerate the forward calculation, we compute numerical first-order partial derivatives relative to each model parameter. Given the range of model space explored, the use of first-derivatives is sufficiently accurate [*James and Ritzwoller*, 1999; *Shapiro and Ritzwoller*, 2002]. For every spatial location, we start from the reference model described above,  $\mathbf{p}_{\text{ref}}$ , and the corresponding Rayleigh or Love wave dispersion curves,  $\mathbf{D}_{\text{ref}}$ , and the partial derivatives ( $\partial \mathbf{D} / \partial p_i$ ) are computed numerically for all 16 free parameters using the MINEOS code. With these partial derivatives, dispersion curves  $\mathbf{D}$  for any model  $\mathbf{p}$  may be approximated as

$$\mathbf{D} = \mathbf{D}_{\text{ref}} + \sum_i \left( \frac{\partial \mathbf{D}_{\text{ref}}}{\partial p_i} \right) \delta p_i \quad (1)$$

where  $\delta p_i = p_i - p_{\text{ref},i}$ , is the perturbation to model parameter  $i$ .

[24] The model space sampling process is guided by the Metropolis law, and goes as follows. Within the model space defined by the prior information, an initial model  $m_0$  is

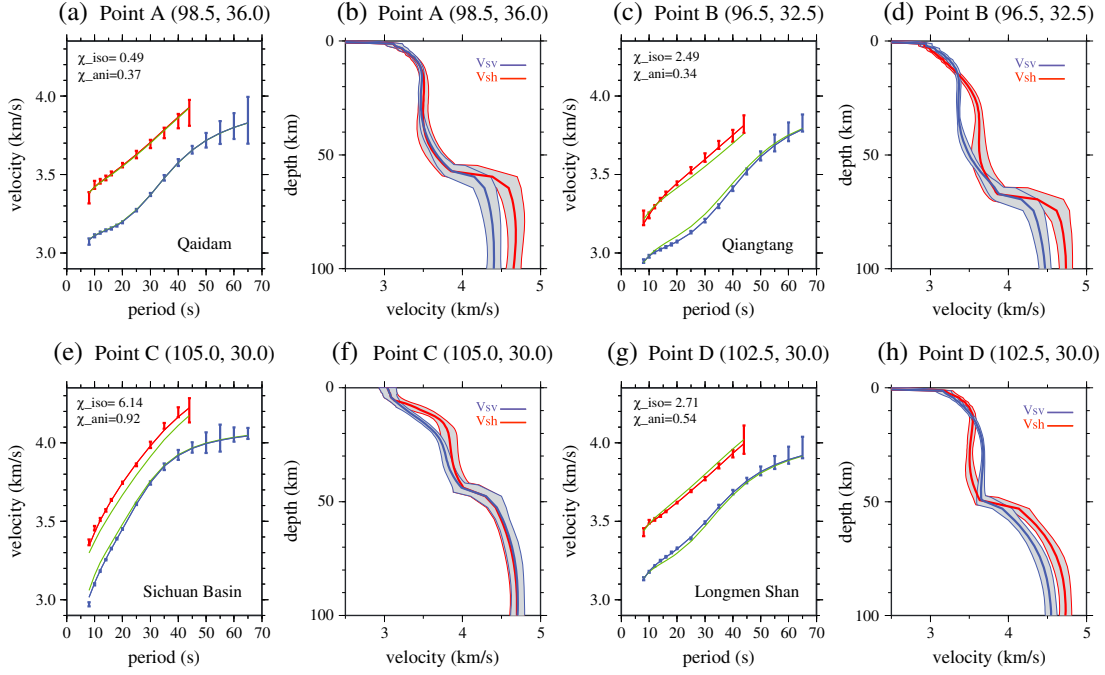


**Figure 7.** Examples of dispersion curves and estimated radially anisotropy for four spatial locations (A, B, C, and D) identified in Figure 1a. (a) Point A (98.5, 36.0) near the eastern edge of the Qaidam Basin. Local Rayleigh and Love wave phase speed curves presented as one-standard deviation ( $1\sigma$ ) error bars. Predictions from the average of the anisotropic model distribution in Figure 7b are shown as solid lines, and green lines are predictions from the Voigt-averaged isotropic  $V_s$  model. Misfits (defined as  $\chi = \sqrt{S/N}$  where  $S$  is defined in equation (3)) correlated with anisotropic and isotropic models are shown at the upper left corner. (b) Point A (cont.). Inversion result in which the one-standard deviation ( $1\sigma$ ) model distributions are shown with the gray corridors for  $V_{sh}$  and  $V_{sv}$ , with the average of each ensemble plotted with bold blue ( $V_{sv}$ ) and red ( $V_{sh}$ ) lines. The model ensembles are nearly coincident in the crust, consistent with an isotropic crust. (c and d) Point B (96.5, 32.5) in the Qiangtang terrane where the central crust has strong positive radial anisotropy between 20 and 50 km depth and weak negative anisotropy above about 15 km depth. (e and f) Point C (105.0, 30.0) in the Sichuan Basin where the central crust has strong positive radial anisotropy between depths of 10 and 25 km. (g and h) Point D (102.5, 30.0) between Tibet and the Sichuan Basin where the central crust has strong negative radial anisotropy between 20 and 50 km depth.

chosen randomly from the prior distribution, and its likelihood function  $L(m_0)$  is computed

$$L(m) = \exp\left(-\frac{1}{2}S(m)\right) \quad (2)$$

where

$$S(m) = S_{\text{Rayleigh}} + S_{\text{Love}} \\ = \sum_i \frac{(D(m)_i^{\text{pred}} - D_i^{\text{obs}})^2}{\sigma_i^2} + \sum_i \frac{(D'(m)_i^{\text{pred}} - D_i^{\text{obs}})^2}{\sigma_i'^2} \quad (3)$$

where  $D(m)_i^{\text{pred}}$  is the predicted phase velocity for model  $m$  at period  $i$  (computed from (1)), and  $D_i^{\text{obs}}$  is the observed phase velocity. Here,  $D$  represents Rayleigh wave phase velocities and  $D'$  indicates Love wave phase velocities. Standard deviations of the Rayleigh and Love wave phase velocity measurements are given by  $\sigma$  and  $\sigma'$ , respectively.

[25] A new model  $m_i$  is generated by perturbing the initial model  $m_0$  following the procedure described by Shen *et al.* [2013b]. The likelihood function  $L(m_i)$  is obtained through a similar computation as described above. The model  $m_i$  is

accepted or rejected according to a probability function  $P$  defined as follows:

$$P_{\text{accept}} = \min(1, L(m_i)/L(m_0)) \quad (4)$$

[26] If  $m_i$  is not accepted, a new  $m_i$  is generated by perturbing the initial model  $m_0$ ; this perturbation continues until a  $m_i$  is accepted. If  $m_i$  is accepted, the next model sampled in model space will be based on it rather than  $m_0$ . This sampling process repeats until the likelihood function levels off, after which a new initial model is chosen randomly from the prior distribution. The process is continued until at least 5000 models have been accepted from at least five initial starting points. We then calculate average values of each parameter in the  $>5000$  accepted models and take that average as a new reference model, and then recalculate dispersion curves and partial derivatives. With this new reference model and a similar sampling procedure, we repeat the process until we find an additional 5000 models accepted from at least 10 initial starting points. The use of various initial models minimizes the dependence on the initial parameters, but we find that initial model dependence is weak. That is, convergence



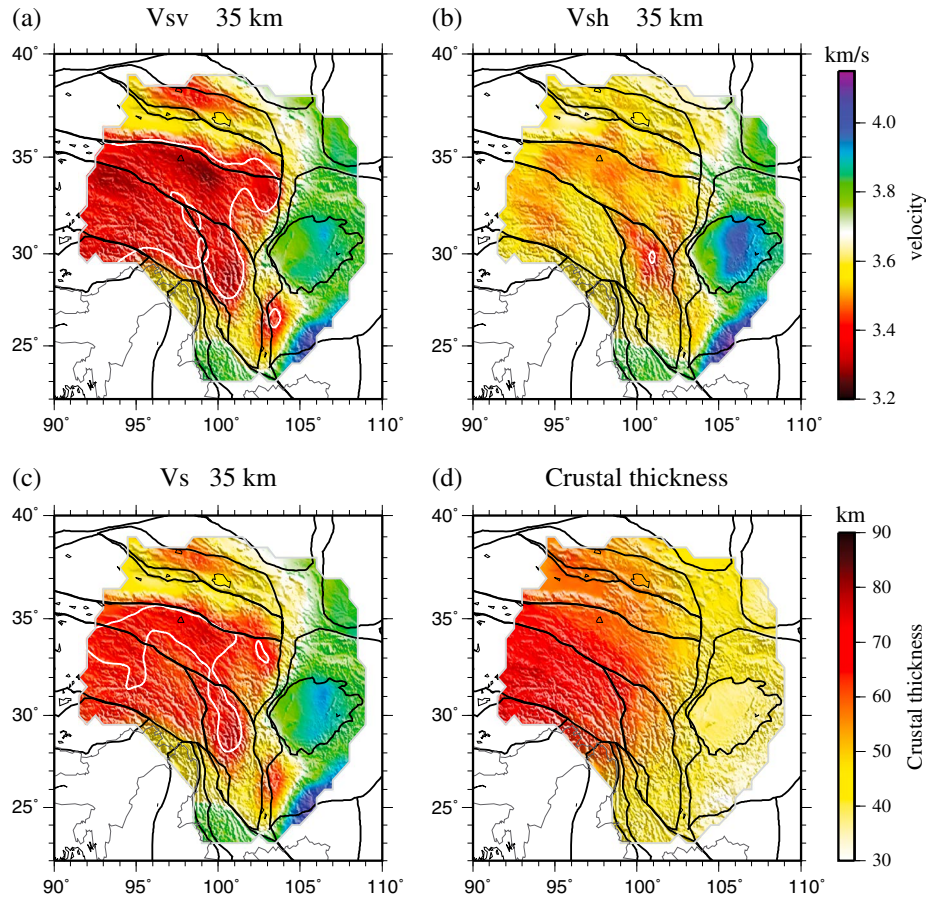


**Figure 8.** The average of the posterior distributions of (a)  $V_{sv}$ , (b)  $V_{sh}$ , and (c)  $V_s$  at 35 km depth in km/s, which is in the middle crust beneath the Tibetan Plateau. Regions with very low velocities ( $<3.4$  km/s) are encircled by white contours. (d) The average of the posterior distribution of crustal thickness in kilometers.

tends to be to similar models irrespective of the initial model starting point.

[27] The use of partial derivatives aims to accelerate computations during the process of identifying acceptable models in the Monte Carlo search. In order to eliminate possible bias caused by the use of the partial derivatives, the Rayleigh and Love wave phase velocity curves are recomputed for each accepted model using MINEOS when the algorithm terminates at each location. This recomputation of the dispersion curves actually takes longer than the entire Monte Carlo search, but there is little difference between the dispersion curves computed with MINEOS and the partial derivatives. This justifies reliance on the partial derivatives to save computation time without sacrificing accuracy.

[28] The Monte Carlo sampling will generate an ensemble of anisotropic models that fit the data better than the reference model. The ensemble is reduced further in size by an additional acceptance criterion defined as follows:

$$\chi \leq \begin{cases} \chi_{\min} + 0.5 & \text{if } \chi_{\min} < 0.5 \\ 2\chi_{\min} & \text{if } \chi_{\min} \geq 0.5 \end{cases}$$

where misfit  $\chi = \sqrt{S/N}$  is the square root of reduced chi-squared value,  $S$  is misfit defined by equation (3), and  $N$  is the number of observed data (number of discrete points along the Rayleigh and Love wave phase velocity curves).

Thus, on average, this posterior distribution includes models whose misfit is less than about twice that of the best-fitting model, which has a square root of reduced chi-squared value of  $\chi_{\min}$ .

[29] Finally, the mean and standard deviation of  $V_{sv}$  and  $V_{sh}$  are used to summarize the posterior distribution for each depth and location. As an example, consider point B (Figure 1a), where midcrustal anisotropy is needed to fit the data (Figure 6). The widths of the posterior distributions reflect how well  $V_{sv}$ ,  $V_{sh}$ , and their differences are constrained at each depth. Uncertainties in shear wave speeds at depths of 20 and 35 km are less than about 50 m/s, but are about twice as large at 50 km. Moreover, radial anisotropy is inescapable at 20 and 35 km depth, but not required, if still likely, at 50 km. The poorer resolution at 50 km results from the lack of long-period Love wave data, increasing data uncertainties with period, and the trade-off between lower crustal and uppermost mantle structures. Therefore, as mentioned earlier, we mainly focus discussion on structures no deeper than about 50 km.

[30] We performed the Bayesian Monte Carlo inversion at every grid point in the study region to produce posterior distributions. In section 4, we present the spatial variations in the means and standard deviations of the distribution. Then in section 5, we query the entire distribution to address particular scientific questions.

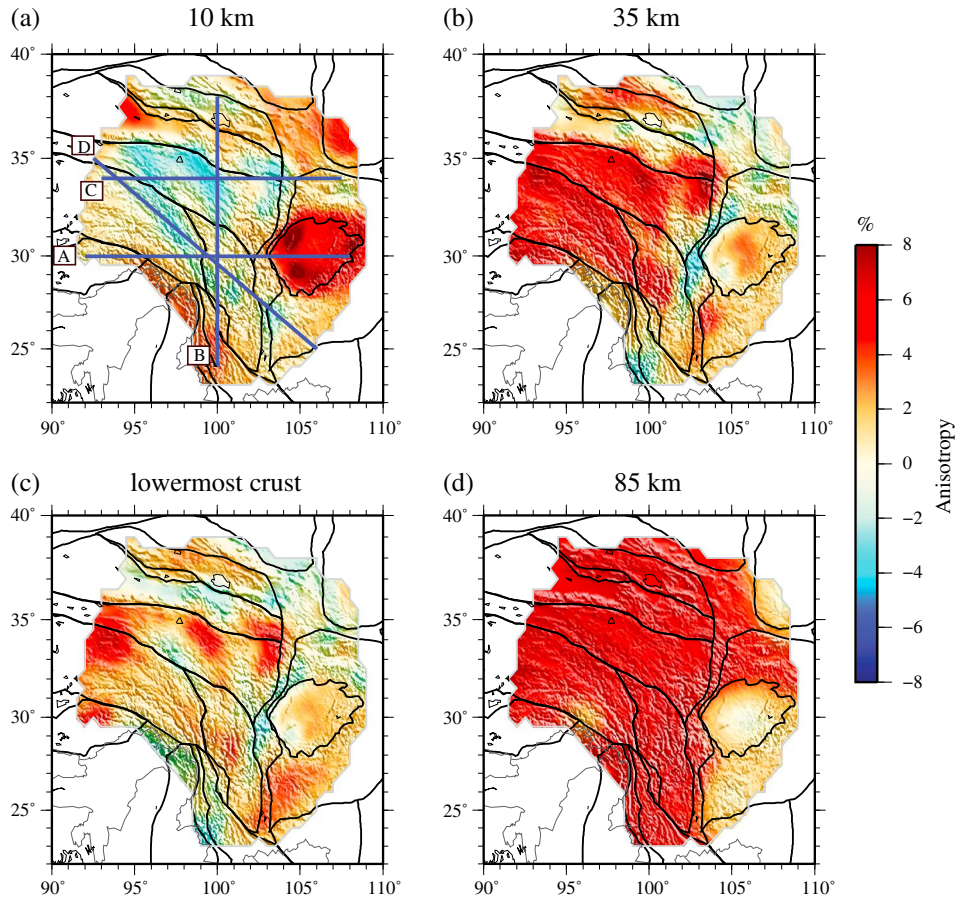


**Figure 9.** Maps of the mean of the posterior distribution for estimates of radial anisotropy at (a) 10 km depth, (b) 35 km depth, (c) 90% of the depth to Moho in the lowermost crust, and (d) 85 km depth. Radial anisotropy is the percent difference between  $V_{sh}$  and  $V_{sv}$  at each location and depth ( $\gamma$ ), and  $V_s$  is the Voigt-averaged shear wave speed. Blue lines in Figure 9a identify the locations of the vertical cross sections in Figure 10.

## 4. Inversion Results

### 4.1. Example Results at Various Locations

[31] As examples of local dispersion curves and the results of their inversion to produce a radially anisotropic model, we consider results at four locations in different parts of eastern Tibet and its surroundings (Figure 1a, points A–D). For point A, which is north of the Kunlun fault near the eastern edge of the Qaidam Basin, the gray-shaded areas of the inverted model representing the  $1\sigma$  uncertainty of the posterior distribution of accepted models in  $V_{sh}$  and  $V_{sv}$  (Figure 7b) give no indication of crustal radial anisotropy.  $V_{sh}$  and  $V_{sv}$  are approximately equal in the crust, and no Rayleigh-Love discrepancy is observed (Figure 7a). In contrast, for point B in the middle of eastern Tibet, a strong Rayleigh-Love discrepancy is seen for all isotropic models (Figure 7c), and large differences are required in  $V_{sh}$  and  $V_{sv}$  between  $\sim 20$  and 50 km depth, as large as  $7.8\% \pm 1.6\%$  (Figure 7d). The model uncertainty increases near the base of the sedimentary layer (not shown) and near the Moho, which reflects the velocity-depth trade-off near interfaces characteristic of surface wave inversions. This prevents precise imaging of the discontinuities using surface waves alone. Although the inversion is performed to a depth of 200 km, we

concentrate discussion on the crust where radial anisotropy is well resolved.

[32] For point C in the Sichuan Basin, the Rayleigh and Love wave dispersion curves (Figure 7e) call for anisotropy only in the upper 20 km of crust (Figure 7f). As discussed in section 4.3, the anisotropy could be confined to the sediments but would need to be about four times stronger. For point D in the Longmenshan region between Tibet and the Sichuan Basin, midcrustal radial anisotropy is required, but in this case  $V_{sv} > V_{sh}$  and radial anisotropy is negative.

[33] In Figure 7, green lines on the dispersion curves represent the predicted curves for the best-fitting isotropic  $V_s$  model in the crust, although the mantle contains radial anisotropy. They show the observed Rayleigh-Love discrepancy, how the best-fitting isotropic model misfits the data at points B, C, and D where radial anisotropy is required in the middle crust.

### 4.2. Maps of $V_{sv}$ , $V_{sh}$ , and Voigt-Averaged $V_s$

[34] Maps of the mean of the resulting posterior distributions for  $V_{sv}$ ,  $V_{sh}$ , and the Voigt-averaged isotropic  $V_s$  in the middle crust of Tibet ( $\sim 35$  km) are shown in Figure 8, in addition to the mean of crustal thickness. The most

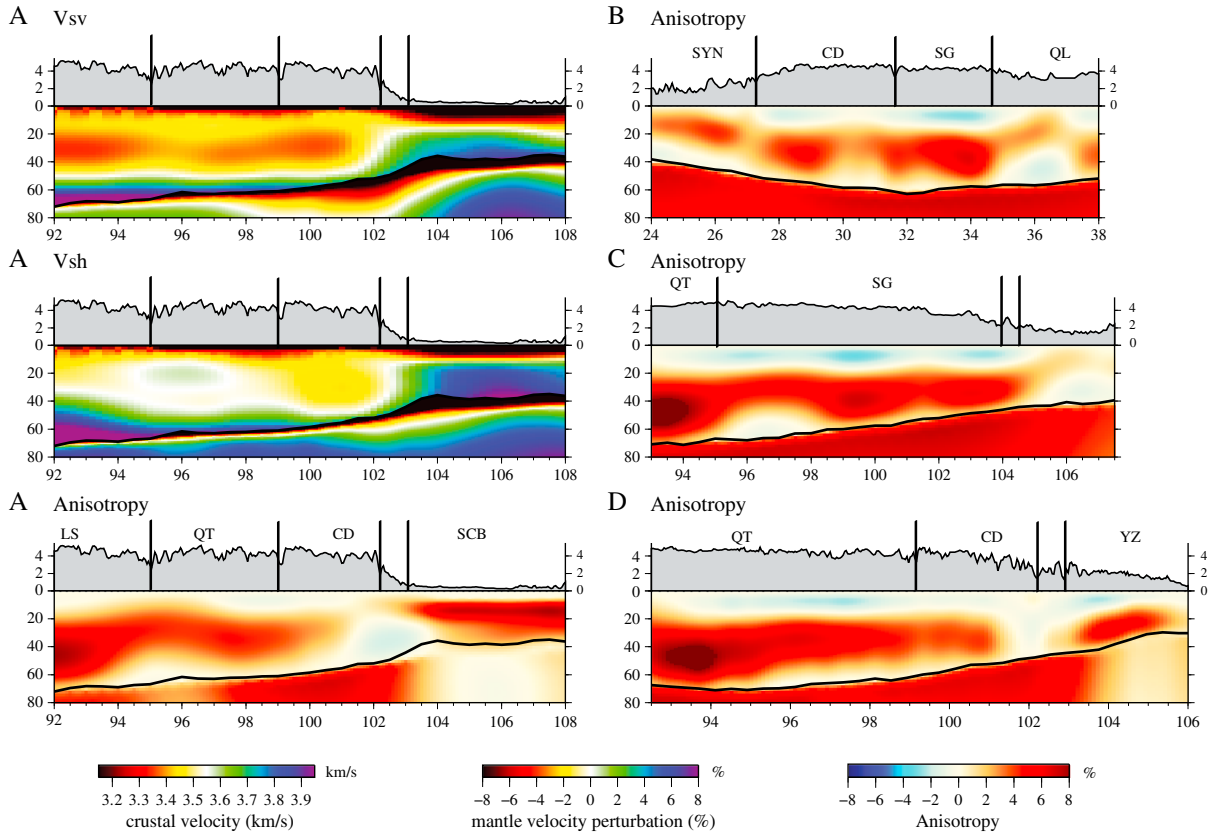


**Figure 10.** Vertical cross sections of (top left)  $V_{sv}$ , (middle left)  $V_{sh}$ , and (bottom left)  $V_s$  radial anisotropy  $\gamma$  along profile A (Figure 9a) taken from the mean of the posterior distribution at each location and depth. Topography is shown at the top of each panel as are locations of geological-block boundaries (SG: Songpan-Ganzi terrane, CD: Chuandian terrane, LS: Lhasa terrane, QL: Qilian terrane, SCB: Sichuan Basin, SYN: South Yunnan region, YZ: Yangtze craton). Crustal shear velocities are presented in absolute units (km/s),  $V_s$  radial anisotropy is presented as the percent difference between  $V_{sh}$  and  $V_{sv}$  ( $\gamma$ ), and mantle velocities are percentage perturbations relative to 4.4 km/s. (right column)  $V_s$  radial anisotropy is presented beneath profiles B, C, and D (Figure 9a).

prominent feature is the low midcrustal shear wave speed across all of eastern Tibet compared with much higher speeds outside of Tibet. In the midcrustal  $V_{sv}$  map (Figure 8a), anomalies are similar to those presented in an earlier study using a similar data set [Yang *et al.*, 2012]. The  $V_{sh}$  model is faster than  $V_{sv}$  across the high plateau, indicating strong positive radial anisotropy. Combining  $V_{sv}$  and  $V_{sh}$ , an isotropic  $V_s$  estimate is computed from the Voigt averaging method mentioned in section 1. In these maps, white contours outline regions with shear wave speeds lower than 3.4 km/s, below which partial melting may be expected to exist [e.g., Yang *et al.*, 2012]. Although  $V_{sv} < 3.4$  km/s exists across much of eastern Tibet,  $V_{sh} > 3.4$  km/s is present across the majority of the region. The difference between  $V_{sv}$  and  $V_{sh}$  causes the white contour in the  $V_s$  map to contract toward the interior of eastern Tibet in the  $V_s$  map, predominantly within the Songpan-Ganzi and the northern Chuandian terrane. This feature of the  $V_s$  model is discussed further in section 5.

### 4.3. Radial Anisotropy

[35] From the posterior distributions of  $V_{sv}$  and  $V_{sh}$  at each location, we obtain the radial anisotropy model. Radial

anisotropy at different depths and along different vertical profiles is shown in Figures 9 and 10. In this section, we first discuss the distribution of radial anisotropy qualitatively, and then the estimated uncertainties are presented and discussed in section 4.4.

[36] In the upper crust (Figure 9a), radial anisotropy beneath the Tibetan Plateau is negative, on average. Beneath the Sichuan Basin, in contrast, it is positive with amplitudes in excess of 6%. Actually, the depth extent of the strong upper crustal radial anisotropy beneath the Sichuan Basin is not well constrained by the data. For example, it could also have been confined to the sediments, but in this case, radial anisotropy of about 25% would be needed to fit the data. Because of this exceptionally large amplitude, we prefer a model with radial anisotropy confined to the upper crystalline crust.

[37] In the middle crust (Figure 9b), relatively strong positive radial anisotropy with amplitudes ranging from 4% to 8% is observed across most of eastern Tibet, where the strongest anisotropy is concentrated near the northern margin of the Qiangtang terrane. Near the northern and eastern margins of the Tibetan Plateau, radial anisotropy decreases in amplitude. To the north, radial anisotropy decreases abruptly across the Kunlun fault, and to the east, radial anisotropy

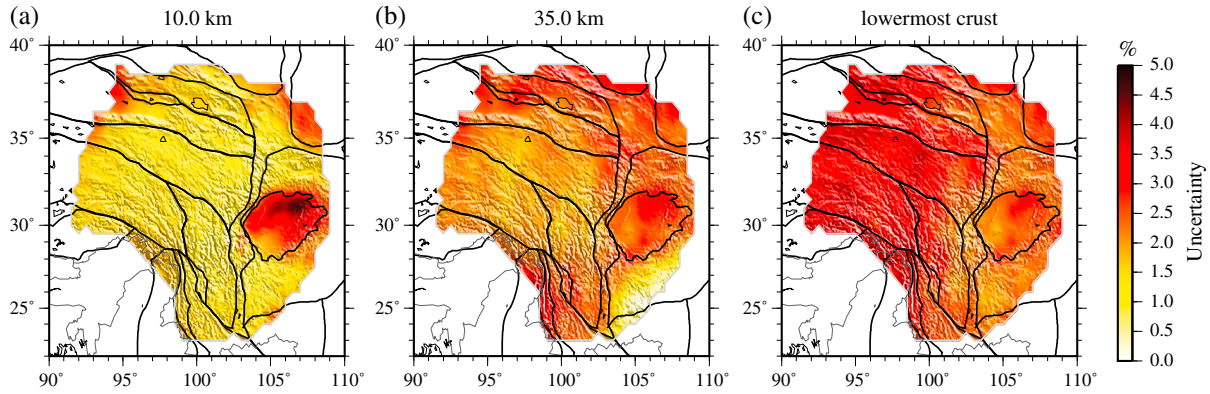


**Figure 11.** Maps of the one-standard deviation (i.e., error) of the posterior distribution for estimates of  $V_s$  radial anisotropy at (a) 10 km depth, (b) 35 km depth, and (c) 90% of the depth to Moho. Results are in the same units as radial anisotropy, not in the percentage of radial anisotropy at each point.

decreases and becomes negative near the Longmenshan west of the Sichuan Basin. The northern margin of radial anisotropy closely follows the Kunlun fault. In contrast, the termination of radial anisotropy near the southeastern margin of Tibet does not follow the topography or geological boundaries. Strong radial anisotropy covers only the northern half of the Chuandian terrane, and it ends before the plateau drops off and topography decreases. To the east of the Tibetan Plateau, negative radial anisotropy shows up near the Longmenshan, in a narrow strip between the Chuandian terrane and the Sichuan Basin. Outside the Tibetan Plateau, midcrustal radial anisotropy is weak except within and south of the Sichuan Basin and in the Qilian terrane.

[38] In the lower crust (Figure 9c), radial anisotropy is weak across most of the region of study, with notable isolated anomalies in the northern Songpan-Ganzi and Qiangtang terranes. In fact, radial anisotropy at this depth is not determined reliably because anisotropy trades-off with both Moho depth and radial anisotropy in the uppermost mantle. This phenomenon is reflected in the large uncertainties shown in Figure 11c.

[39] In Figure 9d, uppermost mantle anisotropy at 85 km depth is shown, which is taken from the model of *Shapiro and Ritzwoller* [2002], as mentioned in section 3.1. Shapiro's model of anisotropy is fairly uniform across the study region with an average positive anisotropy of  $\sim 6\%$ , but much weaker mantle anisotropy exists within and south of the Sichuan Basin. In fact, weak negative anisotropy exists beneath parts of the Sichuan Basin in their model.

[40] The locations of the four vertical transects are shown in Figure 9a, and the vertical transects themselves are presented in Figure 10. For profile A,  $V_{sv}$ ,  $V_{sh}$ , and radial anisotropy are presented. For profiles B, C, and D, only radial anisotropy is presented.

[41] For profile A,  $V_{sv}$  is similar to the result presented by *Yang et al.* [2012] using a similar data set. Within the high plateau, a  $V_{sv}$  minimum in the middle crust is seen clearly from about 20 to 40 km depth. In the Sichuan Basin, a very slow sedimentary layer is present along with faster lower crust. Compared to  $V_{sv}$ ,  $V_{sh}$  is faster from the surface to the base of the crust except in the uppermost crust of the high plateau and the midcrustal velocity minimum seen for  $V_{sv}$  is much more subtle. There are differences in upper crustal  $V_{sv}$  and  $V_{sh}$  in the Sichuan Basin as well. Radial anisotropy beneath the high plateau along profile A increases from an

average of about  $-1\%$  in the uppermost crust to values of  $4\%$  to  $6\%$  between 20 and 50 km depth. Radial anisotropy then decreases with depth in the lower crust. Near the eastern edge of the plateau, radial anisotropy vanishes as surface elevation falls off, perhaps changing sign before elevation plummets at the Longmenshan.

[42] The three other vertical profiles shown in Figure 10 are similar to profile A in the vertical distribution of radial anisotropy in the crust across the Tibetan Plateau: radial anisotropy is negative, on average, in the uppermost crust, positive and peaks in amplitude in the middle crust, decreases in the lower crust, and terminates near the border of the high plateau except within and south of the Sichuan Basin. The nature of the termination of radial anisotropy near the border of the plateau varies from place to place. For example, in profile C, which runs across the northeastern part of the plateau, radial anisotropy decreases gradually as topography decreases. In contrast, in profile D, which goes through the southeastern part of the plateau, radial anisotropy ends abruptly before topography decreases.

[43] In summary, within the Tibetan Plateau, strong positive radial anisotropy begins at about 20 km depth and peaks between 30 and 50 km depth. It is almost continuous between different terranes, but there is some diminishment in amplitude near terrane boundaries as profile B illustrates. Radial anisotropy has a somewhat broader depth range in the Qiangtang terrane compared with other terranes. Outside of the Tibetan plateau, strong upper-to-middle crustal radial anisotropy shows up in and south of the Sichuan Basin. Negative anisotropy is mostly confined to the uppermost crust beneath Tibet and in the middle crust in the Longmenshan region, near the border between Tibet and the Sichuan Basin.

#### 4.4. Uncertainty in Radial Anisotropy

[44] Figure 11 presents uncertainties in the estimated radial anisotropy in the region of study at depths of 10 and 35 km, as well as in the lower crust at a depth of 90% of crustal thickness. The uncertainty is defined as one-standard deviation of the posterior distribution at each depth. Except beneath the Sichuan Basin, uncertainties grow with depth in the crust because a smaller percentage of the observed dispersion curves are sensitive to the greater depths. Beneath the Sichuan Basin, the higher shallow uncertainties result from the trade-off of shear velocities in the crystalline crust and sediments.

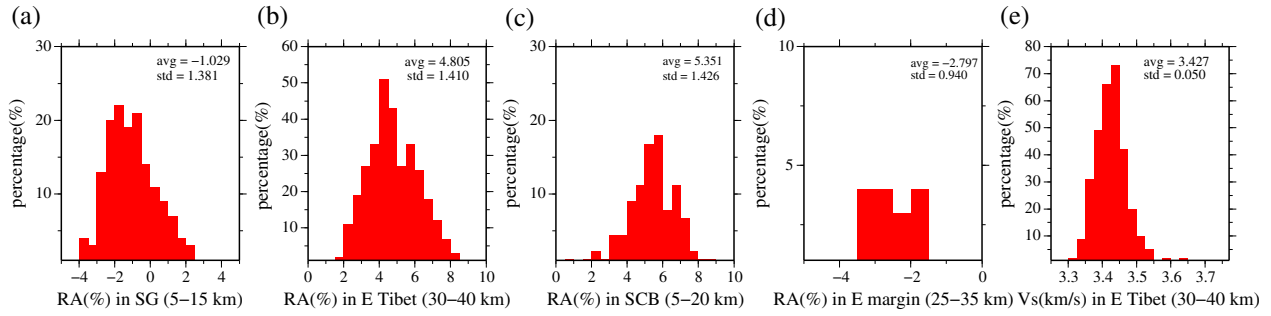


**Figure 12.** Plots of the spatial distribution of the mean of the posterior distributions of  $V_s$  radial anisotropy across (a) the Songpan-Ganzi terrane between depths of 5 and 15 km, (b) eastern Tibet at depths between 30 and 40 km, (c) the Sichuan Basin at depths between 5 and 20 km, and (d) the Longmenshan region between eastern Tibet and the Sichuan Basin between 25 and 35 km. (e) The distribution of the mean of the posterior distribution for Voigt-averaged shear wave speed  $V_s$  across eastern Tibet between depths of 30 and 40 km.

At 10 km depth, the average uncertainty in eastern Tibet is about 1%, whereas in the midcrust it is about 2%, and in the lower crust it is about 3.5%. As discussed in section 5.4.1, if we had not constrained  $V_{sh} = V_{sv}$  for crustal B-splines 1 and 5 (Figure 5) in the uppermost and lowermost crust, uncertainties in radial anisotropy in the uppermost and lowermost crust would have been larger. The higher uncertainties in the lower crust result from the fact that Love waves do not constrain  $V_{sh}$  well at these depths and there are trade-offs with crustal thickness and uppermost mantle structure and that is why we concentrate discussion on shallower depths.

#### 4.5. Computation of Regional Averages

[45] Several of the attributes of the model observed here appear to be fairly homogeneous over extended areas. These attributes include positive midcrustal radial anisotropy beneath eastern Tibet and the Sichuan Basin, negative midcrustal radial anisotropy near the Longmenshan adjacent to the eastern border of Tibet, negative radial anisotropy in the shallow crust beneath parts of eastern Tibet (notably the Songpan-Ganzi terrane), and  $V_s$  in the midcrust beneath eastern Tibet. We present here averages of the means and the standard deviations of the mean of these variables defined over the four regions. These standard deviations, in contrast with those presented in Figure 11 and discussed in section 4.4, principally reflect spatial variations rather than uncertainties.

[46] There are four regions over which we compute the averages. First, we consider “eastern Tibet” to be defined by the interior of the 84.2% probability contour (orange and red colors) of positive midcrustal radial anisotropy near Tibet, which is presented later in the paper (Figure 13a). This contour approximately follows the outline of the high plateau. Second, we consider the Longmenshan region near the border between Tibet and the Sichuan Basin to be contained within the 15.8% probability contour (blue colors) of positive midcrustal radial anisotropy (Figure 13a). Finally, we use the geological outlines of the Sichuan Basin and the Songpan-Ganzi terrane as the third and fourth regions.

[47] In the Songpan-Ganzi terrane, the distribution of the means of shallow crustal ( $\sim 10$  km) radial anisotropy is presented in Figure 12a. The average of the means in this region is  $-1.03\% \pm 1.38\%$ . This is the structural attribute with the relatively largest variability. The distribution of the

means of midcrustal radial anisotropy across eastern Tibet ( $\sim 35$  km) and the Sichuan Basin ( $\sim 15$  km) is presented in Figures 12b and 12c. Midcrustal radial anisotropy averages  $4.81\% \pm 1.41\%$  in eastern Tibet. Across the Sichuan Basin, the average is somewhat larger,  $5.35\% \pm 1.43\%$ . Also in the middle crust, but averaged over the Longmenshan region ( $\sim 30$  km), the distribution of the means of midcrustal radial anisotropy is presented in Figure 12d. The average is  $-2.80\% \pm 0.94\%$ . Finally, midcrustal  $V_s$  averaged over eastern Tibet is  $3.427 \text{ km/s} \pm 0.050 \text{ km/s}$ , as seen in Figure 12e.

#### 5. Identifying Highly Probable Model Attributes

[48] The means of the posterior distributions of the models that result from the Bayesian Monte Carlo inversion of Rayleigh and Love wave dispersion curves have been used to infer that (1) positive ( $V_{sh} > V_{sv}$ ) midcrustal radial anisotropy exists across the entirety of eastern Tibet with an average amplitude ( $\gamma$ ) of about 4.8% ( $\sim 35$  km) and at much shallower depths ( $\sim 15$  km) beneath the Sichuan Basin with an average amplitude of about 5.4%, (2) weaker negative radial anisotropy ( $V_{sh} < V_{sv}$ ) appears in the middle crust ( $\sim 30$  km) along the Longmenshan region ( $-2.8\%$ ) and in the shallow crust ( $\sim 10$  km) across the Songpan-Ganzi terrane ( $-1.03\%$ ), and (3) the Voigt-averaged shear wave speed in the middle crust ( $\sim 35$  km) averages about 3.427 km/s across eastern Tibet. From the geographical spread of the local means of the posterior distributions of these attributes, we have inferred that these observations are characteristic of each region. Radial anisotropy in the lowermost crust is more poorly constrained than at shallower depths because of a trade-off with crustal thickness and radial anisotropy in the mantle.

[49] Although the mean of the posterior distribution is interpreted as its maximum likelihood, the Bayesian Monte Carlo inversion delivers a distribution of models at each depth. For this reason, within a Bayesian framework, the probability that the model achieves a particular attribute can be computed. Here we address the following questions across the region of study: (1) What is the probability that positive ( $V_{sh} > V_{sv}$ ) radial anisotropy exists in the shallow crust or in the middle crust? (2) Similarly, what is the probability for negative radial anisotropy? (3) What is the probability

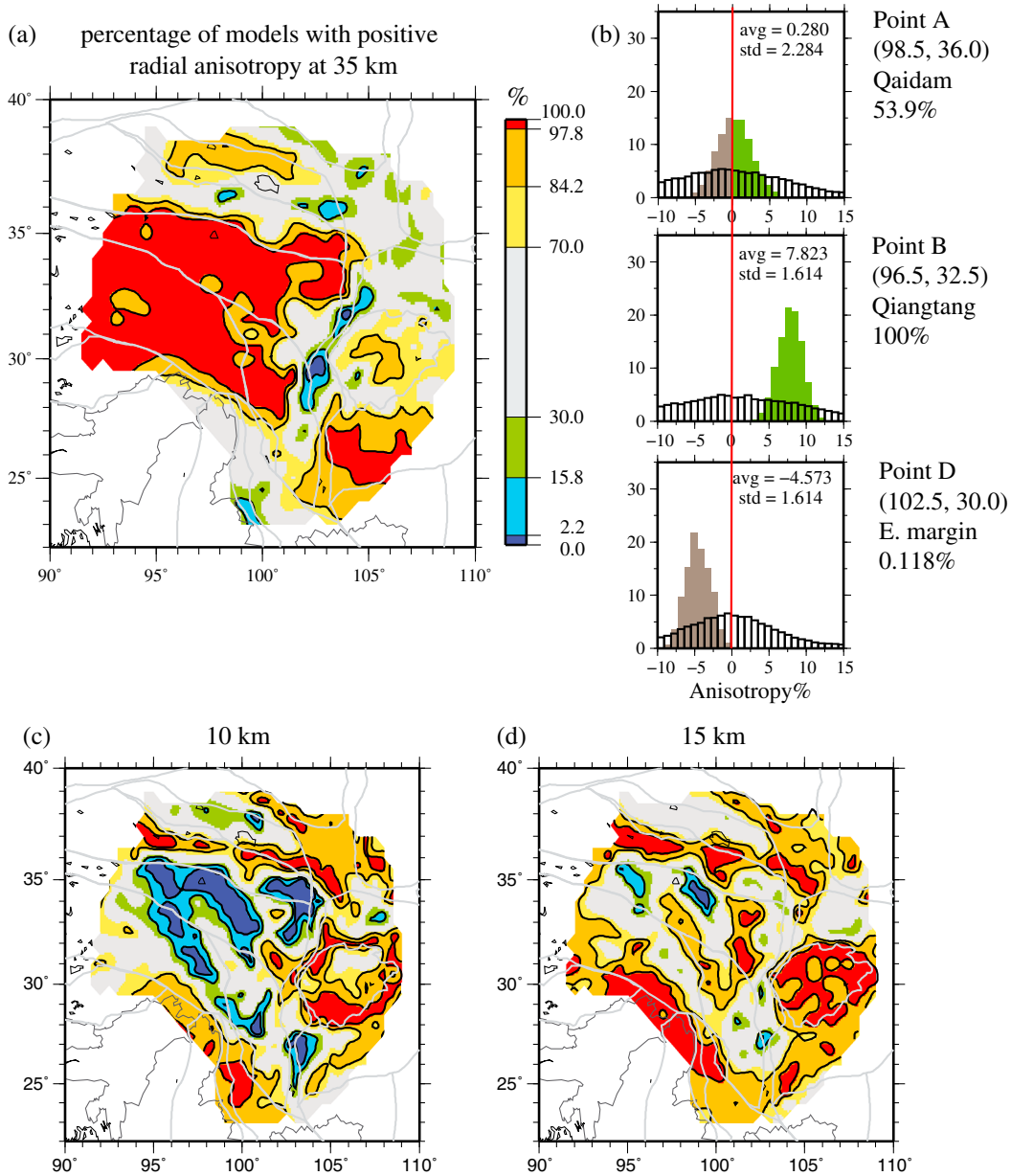


**Figure 13.** (a) Percent of accepted models at each location with positive  $V_s$  radial anisotropy  $\gamma$  ( $V_{sh} > V_{sv}$ ) at 35 km depth. Values of 2.2%, 15.8%, 84.2%, and 97.8% are contoured by black lines, which are correlated with the position of  $\pm 1\sigma$  and  $\pm 2\sigma$  for a Gaussian distribution. (b) Prior (white histogram in the background) and posterior (colored histogram) distributions of  $V_s$  radial anisotropy in percent at 35 km depth for locations A, B, and D of Figure 1a. The red line indicates the position of zero radial anisotropy. The percent of models with positive radial anisotropy is indicated to the right of each panel. (c) Same as Figure 13a, but for positive  $V_s$  radial anisotropy at 10 km depth. (d) Same as Figure 13a, but for positive  $V_s$  radial anisotropy at 15 km depth.

that the Voigt-averaged shear wave speed lies below or above 3.4 km/s in the middle crust?

[50] In computing these probabilities, we acknowledge that the posterior distribution represents a conditional probability in which the likelihood is conditioned on prior information that appears in the range of the model variables allowed, the constraints imposed, the parameterization chosen, the details of the search algorithm, and the assumptions made (e.g.,  $\rho/V_s$ ,  $V_p/V_s$ ,  $Q$ ). From a Bayesian perspective, the distribution represents the authors' degree of belief in the

results, but if the prior information is wrong, then the resulting distribution of models may be biased. In section 5.4, we identify several potential sources for bias and discuss how these choices may affect the mean of the estimated posterior distribution of the selected model attributes.

### 5.1. Computing the Probability of a Model Attribute From the Posterior Distribution

[51] Figures 13a and 13b illustrate the computation of the probability for the existence of positive radial anisotropy in

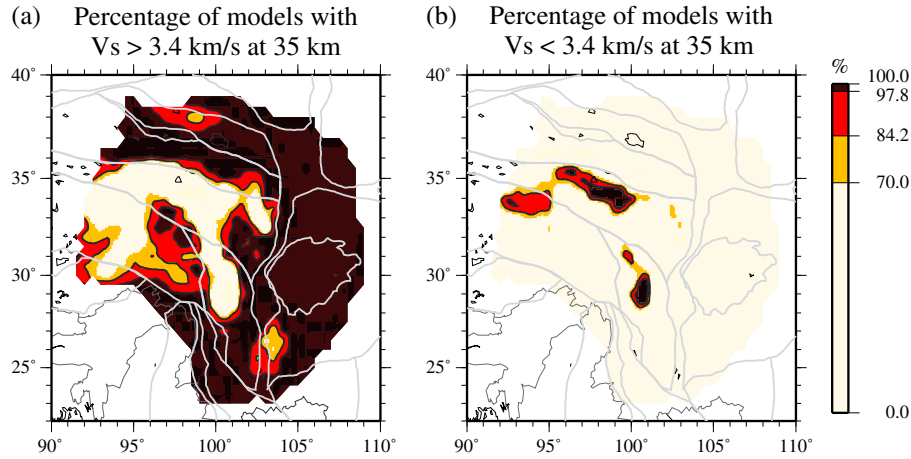


**Figure 14.** (a) Similar to Figure 13a, but this figure is the percentage of accepted models at each location with Voigt-averaged  $V_s > 3.4$  km/s at 35 km depth. (b) Same as Figure 14a, but for  $V_s < 3.4$  km/s at 35 km depth.

the middle crust. The probability that  $V_{sh} > V_{sv}$  (positive radial anisotropy) at 35 km depth is mapped in Figure 13a. It is computed at each point from the local posterior distribution, examples of which are shown for locations A, B, and D from Figure 1a in Figure 13b. For point A, a location that we interpret as isotropic in the crust, approximately half (54%) of the posterior distribution, shows positive anisotropy and half negative. For point B, which we interpret as possessing strong positive midcrustal anisotropy, 100% of the posterior distribution has  $V_{sh} > V_{sv}$  at 35 km depth. For point D, where we observe negative anisotropy on average, only  $\sim 0.12\%$  of the models in the posterior distribution have  $V_{sh} > V_{sv}$ . Thus, at this point, more than 99.8% of the models in the posterior distribution display negative anisotropy in the middle crust.

[52] The values mapped in Figure 13a are simply the percentage of models in the posterior distribution at each point with positive midcrustal radial anisotropy. Examples of the probability of positive radial anisotropy at depths of 10 and 15 km are also shown in Figures 13c and 13d. Similarly, from the local posterior distributions of the isotropic  $V_s$ , the probabilities that  $V_s$  is greater than 3.4 km/s or less than 3.4 km/s are mapped in Figure 14.

[53] In general, we consider a model attribute (e.g.,  $V_{sh} > V_{sv}$  and  $V_s < 3.4$  km/s) to be “highly probable” if it appears in more than 97.8% of the models in the posterior distribution. In this case, all or nearly all of the models in the posterior distribution possess the specified attribute. If the attribute appears in less than 2.2% of the accepted models, then the converse of the attribute (e.g.,  $V_{sh} < V_{sv}$ ,  $V_s > 3.4$  km/s) would be deemed “highly probable.” One could introduce other grades of probability (e.g., probable, improbable, the converse is probable, etc.), but we do not do so here.

## 5.2. Regions With High Probability of Positive or Negative Radial Anisotropy

[54] High probability regions for positive radial anisotropy in the middle crust appear as red colors in Figure 13a and for negative midcrustal anisotropy as dark blue regions. Red colors cover most of eastern Tibet, including the Qiangtang terrane, most of the Songpan-Ganzi terrane, and the northern Chuandian terrane. Another region strongly favoring positive

midcrustal radial anisotropy lies south of the Sichuan Basin, largely in Yunnan province. Midcrustal radial anisotropy has a lower average probability there (orange colors, Figure 13a) than beneath Tibet, because the crust is thinner ( $\sim 40$  km) and at 35 km depth, crustal radial anisotropy trades off with crustal thickness and uppermost mantle radial anisotropy. Blue colors appear in the Longmenshan region near the border of Tibet and the Sichuan Basin, indicating the high probability of negative midcrustal radial anisotropy there.

[55] At shallower depths, the high probability zones of positive or negative radial anisotropy are smaller and more variable than in the middle crust. At 10 km depth (Figure 13c), highly probable negative radial anisotropy is mainly confined to the Songpan-Ganzi terrane but also extends into parts of the Qiangtang and Chuandian terranes. By 15 km (Figure 13d), neither positive nor negative radial anisotropy attains high probabilities pervasively across Tibet, but positive radial anisotropy is highly probable across most of the Sichuan Basin.

## 5.3. Probability of Low Shear Wave Speeds in the Middle Crust

[56] Middle-to-lower crustal low velocity zones (LVZ) have been reported in several studies [e.g., Yao *et al.*, 2008; Yang *et al.*, 2012], but most of these considered  $V_{sv}$  alone. The existence of crustal radial anisotropy with  $V_{sh} > V_{sv}$  across most of eastern Tibet increases the Voigt-averaged shear wave speed relative to  $V_{sv}$  and reduces the strength of a crustal LVZ. Yang *et al.* [2012] argued that 3.4 km/s is a reasonable speed below which partial melt may plausibly begin to occur at a depth of about 35 km depth, although this threshold is poorly known and is probably spatially variable. Other values could also be used. At this depth, the mean value of the Voigt average shear wave speed in the posterior distribution is shown in Figure 8c and the distribution of the mean values across eastern Tibet is presented in Figure 12e. Although shear wave speeds across eastern Tibet average 3.427 km/s, there is substantial spatial variability and the likelihood that  $V_s$  dips below 3.4 km/s in some locations is high.

[57] In the attempt to quantify the likelihood of shear wave speeds less than 3.4 km/s in the middle crust, Figure 14 presents the percentage of models in the posterior distribution

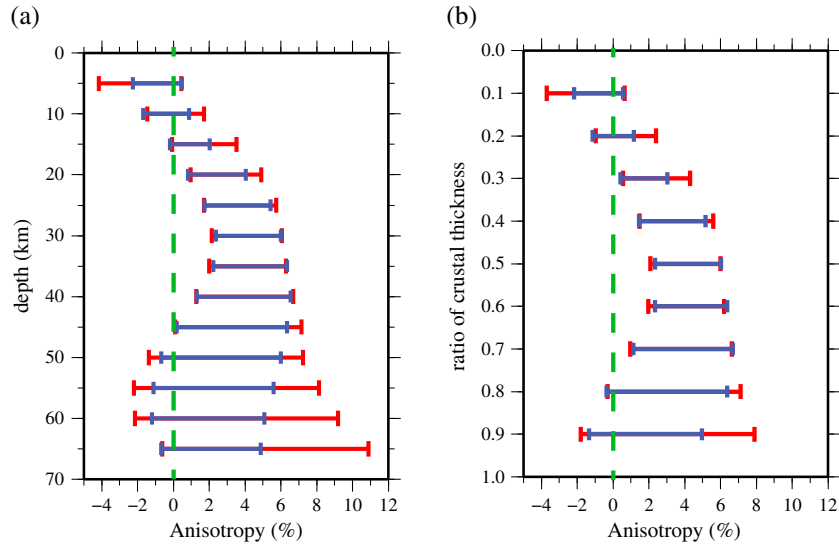


**Figure 15.** The spatially averaged effect of crustal parameterization of radial anisotropy on the mean and standard deviation of  $V_s$  radial anisotropy averaged across the Tibetan crust. Crustal radial anisotropy and uncertainty are presented as error bars as a function of (a) absolute depth and (b) depth measured as a ratio of crustal thickness, averaged over the study region where surface elevation is more than 3 km (black contour in Figure 1a). The middle of each error bar is the average amplitude of  $V_s$  radial anisotropy in percent, and the half-width of the error bar is the average one-standard deviation uncertainty. Blue bars result from the more tightly constrained inversion (uppermost and lowermost crust are approximately isotropic,  $V_{sh} = V_{sv}$  for crustal B-splines 1 and 5 in Figure 5, but  $V_{sh}$  and  $V_{sv}$  can differ for splines 2 to 4). Red bars are results from the less constrained inversion (radial anisotropy is allowed across the entire crust,  $V_{sv}$  may differ from  $V_{sh}$  for all five crustal B-splines).

at each point with  $V_s > 3.4$  km/s and  $V_s < 3.4$  km/s at 35 km depth. As Figure 14a shows,  $V_s > 3.4$  km/s is highly probable across most of the study region, but does not rise to the level of high probability across much of Tibet. Conversely, Figure 14b shows that  $V_s < 3.4$  km/s at this depth is also not highly probable across most of the high plateau. Unfortunately, this means that we cannot infer with high confidence either that midcrustal  $V_s$  is greater than or less than 3.4 km/s across much of Tibet. However, there are two disconnected regions where more than 97.8% of the accepted models have  $V_s < 3.4$  km/s, such that we would infer the high probability of  $V_s < 3.4$  km/s. These regions are in the northern Songpan-Ganzi terrane near the Kunlun fault and in the northern Chuandian terrane. A third region of low  $V_s$  that nearly rises to the level of high probability lies in the northern Qiangtang terrane.

#### 5.4. Caveats: Quantifying the Potential for Bias in the Posterior Distribution

[58] Measurements of midcrustal radial anisotropy, particularly its amplitude, and of shear wave speed  $V_s$ , particularly the minimum value it attains in the middle crust, are affected by a variety of information introduced in the inversion, including the parameterization of crustal radial anisotropy, crustal thickness in the reference model, the fixed amplitude of radial anisotropy in the mantle, the fixed value of the  $V_p/V_s$  ratio in the crust, and the fixed zero amplitude of  $V_p$  radial anisotropy and  $\eta = 1$  in the crust. Errors in these assumptions could bias the posterior distribution and introduce a systematic error that may bias the probability estimates presented in sections 5.1 to 5.3. We discuss here the effects of these

assumptions and also discuss and then dismiss the possibility of overtones, particularly from Love waves, interfering with the estimation of radial anisotropy using fundamental modes.

##### 5.4.1. Relaxing Constraints on Radial Anisotropy in the Uppermost and Lowermost Crust

[59] All results presented above include the constraint that  $V_{sh} = V_{sv}$  for the crustal B-splines 1 and 5 (Figure 5). Figure 15 shows the range of the means of the posterior distributions for radial anisotropy averaged across the high plateau with this constraint applied (blue bars). This is compared with a similar spatial average computed without the constraint (red bars), so that the number of unknowns increases from 16 to 18. The less constrained inversion approximately encompasses the more tightly constrained result. The relaxation of the constraint on radial anisotropy increases the variability of the model, particularly in the uppermost and lowermost crust, and shifts the mean of the distribution in the lowermost crust to larger values. Between depths of 25 and 45 km, however, the means of the distributions are nearly indistinguishable, implying that this constraint does not bias estimates of midcrustal radial anisotropy.

##### 5.4.2. Crustal Thickness and Mantle Radial Anisotropy

[60] The crustal thickness in the reference model (around which the Monte Carlo search occurs) and the fixed amplitude of radial anisotropy in the mantle do affect aspects of the posterior distribution in the middle crust, including the amplitude of radial anisotropy and the isotropic shear wave speed. The effects of these properties of the deeper parts of the model will be stronger, however, where the crust is thinner. This is reflected in the uncertainties in midcrustal radial anisotropy shown in Figure 11b. Uncertainties are smaller



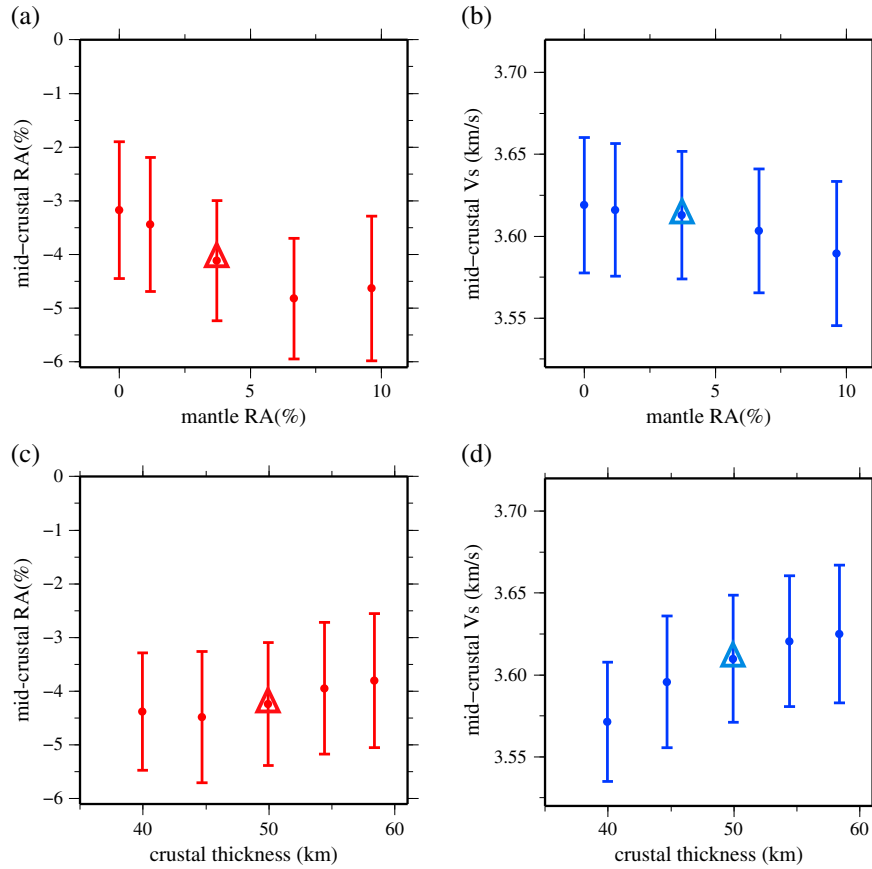


**Figure 16.** Trade-off between the depth-averaged (from Moho to 150 km) mantle Vs radial anisotropy used in the inversion and (a) the depth-averaged ( $\pm 5$  km around the middle crust) midcrustal Vs radial anisotropy and (b) the depth-averaged ( $\pm 5$  km around the middle crust) midcrustal Voigt-averaged Vs. Each dot is the depth-averaged value, and half-widths of the error bars are the depth-averaged one-standard deviation uncertainty. Both come from the inversion with the given mantle radial anisotropy at location D identified in Figure 1a. The triangles are the values in our final model. (c and d) Similar to Figures 16a and 16b, but showing the trade-off between the crustal thickness and the depth-averaged midcrustal Vs radial anisotropy and the depth-averaged midcrustal Voigt-averaged Vs.

across eastern Tibet ( $\sim 1.75\%$ ) where the crust is thicker than in adjacent regions outside Tibet ( $2.0\text{--}3.0\%$ ). Indeed, we find that changes in crustal thickness in the reference model and in the fixed amplitude of radial anisotropy in the mantle do not strongly and systematically affect either the amplitude of radial anisotropy or isotropic Vs in the middle crust beneath eastern Tibet. However, these changes do have a systematic impact on these model attributes where the crust is thinner, for example, in the Longmenshan region near the border of Tibet and the Sichuan Basin. For this reason, we present results here of the impact of changing crustal thickness in the reference model and the amplitude of mantle radial anisotropy at location D (Figure 1a) in the Longmenshan region.

[61] Figures 16a and 16b present the estimates of depth-averaged ( $\pm 5$  km around the middle crust) midcrustal radial anisotropy as well as depth-averaged midcrustal Vs, which result by changing the fixed amplitude of mantle radial anisotropy averaged from Moho to 150 km depth. Error bars reflect the one-standard deviation variation in the posterior distribution in each of the inversions, which are performed identically to the inversions used to produce the model described earlier in the paper (which is the middle error bar

with a triangle in the center in Figures 16a and 16b). The effect of mantle radial anisotropy on Vs is very weak, but increasing mantle radial anisotropy does systematically reduce crustal radial anisotropy. Changing the depth-averaged mantle radial anisotropy from about 4% to 0% or 10% changes the estimated depth-averaged crustal radial anisotropy by less than  $\pm 1\%$ , however. Because we believe that mantle radial anisotropy is probably known better than this range, this possible systematic shift in crustal radial anisotropy is probably an overestimate. Still, it lies within the stated errors of crustal radial anisotropy in the Longmenshan region. If potential systematic errors lie within stated uncertainties, we consider them not to be the cause for concern.

[62] Similarly, Figures 16c and 16d present estimates of depth-averaged ( $\pm 5$  km around the middle crust) midcrustal radial anisotropy and depth-averaged midcrustal Vs caused by changing crustal thickness in the reference model. Again, the middle error bar is the result of the inversion for the model presented earlier in this paper, so that in the Longmenshan region the crustal thickness of the reference model was about 50 km. Changing the crustal thickness in the reference model (around which the Monte Carlo inversion searches) from 40

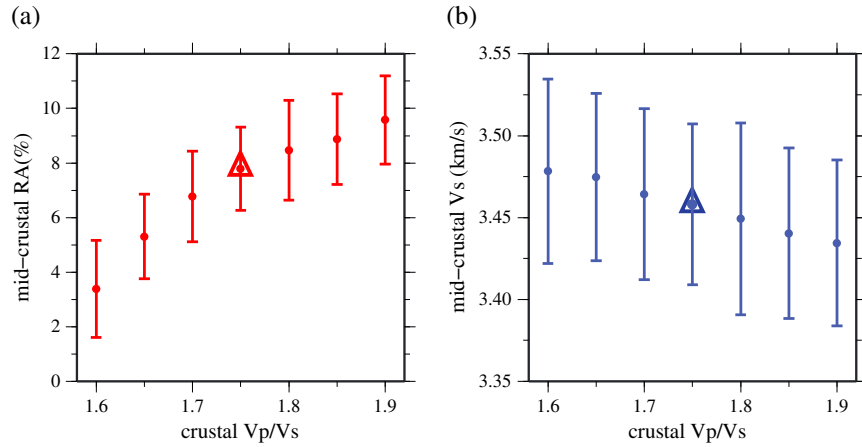


**Figure 17.** Similar to Figure 16, but shows the trade-off between the fixed value of the crustal Vp/Vs used in the inversion and (a) the depth-averaged (from 30 to 40 km) crustal Vs radial anisotropy and (b) the depth-averaged (from 30 to 40 km) midcrustal Voigt-averaged Vs. Values are from inversion with the given crustal Vp/Vs at location B identified in Figure 1a.

to 60 km has a systematic effect both on crustal radial anisotropy and midcrustal isotropic Vs. But, again, the effect is relatively small ( $\pm 0.5\%$  in midcrustal radial anisotropy,  $\pm 25$  m/s in midcrustal Vs). Although the range of crustal thickness considered is considerably larger than what we consider physically plausible for this location, the effect on model characteristics is below the stated model uncertainty.

[63] Therefore, both midcrustal Vs and the midcrustal radial anisotropy are affected by the fixed amplitude of mantle radial anisotropy and the crustal thickness in the reference model, but the effects are below estimated model uncertainties and could only become significant if the effects were correlated and would add constructively. Although this is possible, in principle, it is unlikely to occur systematically across the region. Tighter constraints on crustal thickness and mantle radial anisotropy would result from the joint interpretation of receiver functions and longer period dispersion measurements from earthquakes. Uncertainties in these quantities, therefore, are expected to reduce over time, but we believe that these improvements will not change the results presented here appreciably.

#### 5.4.3. Vp/Vs in the Crust

[64] The strongest and also the most troubling parameter that may produce a systematic error in estimates of radial anisotropy is crustal Vp/Vs, which has been fixed in the crust at Vp/Vs = 1.75, the value for a Poisson solid which is generally considered to be typical of continental crust [Zandt and Ammon, 1995; Christensen, 1996]. Although normal Vp/Vs ( $\sim 1.75$ ) has been widely observed across much of eastern Tibet [Vergne *et al.*, 2002; Xu *et al.*, 2007a, 2007b; Wang *et al.*, 2010; Mechie *et al.*, 2011, 2012; Yue *et al.*, 2012], very low crustal Vp/Vs values also have been observed in the northern Songpan-Ganzi terrane [Jiang *et al.*, 2006], and very high crustal Vp/Vs has been observed near the Kunlun fault [Vergne *et al.*, 2002], the eastern margin of the plateau [Xu *et al.*, 2007a, 2007b; Wang *et al.*, 2010], as well as parts of the Qiangtang terrane [Yue *et al.*, 2012]. Thus, the assumption of uniform Vp/Vs across all of Tibet may be inappropriate.

[65] To test the effect of the assumption that crustal Vp/Vs = 1.75 on the amplitude of midcrustal radial anisotropy, we have inverted with different crustal Vp/Vs ratios and

have plotted the resulting depth-averaged midcrustal radial anisotropies for point B (Figure 1a) in Figure 17a. We apply these tests at a point in eastern Tibet, in contrast with the tests presented in section 5.4.2, which were for the Longmenshan region. Positive correlation is observed between the applied crustal Vp/Vs and depth-averaged radial anisotropy, and midcrustal radial anisotropy may become zero when Vp/Vs drops below 1.60. This extremely low Vp/Vs could exist at depths where the Alpha-Beta quartz transition occurs, namely in a thin layer that occurs somewhere between 20 and 30 km depth [Mehie *et al.*, 2011]. Also, relatively low crustal Vp/Vs may be caused by crust with a felsic composition [Mehie *et al.*, 2011]. However, both alternatives are for a thin low Vp/Vs layer, not the whole crust, and it is physically unlikely to have an average crustal Vp/Vs of 1.60. With values of Vp/Vs ranging from 1.70 to 1.80, the effect is to change the amplitude of radial anisotropy only by about  $\pm 1\%$ . Although radial anisotropy is required across eastern Tibet, the reliability of estimates of its amplitude would be improved with better information about Vp/Vs across Tibet.

[66] The value of crustal Vp/Vs not only affects the amplitude of crustal radial anisotropy but also the shear wave speed (Vs). Figure 17b shows that crustal Vp/Vs and depth-averaged midcrustal Vs are anticorrelated, with Vs decreasing as crustal Vp/Vs increases. This result may seem counterintuitive. With a fixed Vp/Vs, increasing radial anisotropy will increase Vs. In addition, increasing Vp/Vs tends to increase radial anisotropy. Nevertheless, increasing Vp/Vs in the inversion reduces the inferred Vs because increasing Vp at a constant Vs increases the Rayleigh wave speed but not the Love wave speed. In this case, Vsv must be lowered to reduce the Rayleigh-Love discrepancy. The lowering of Vsv (caused by increasing Vp/Vs) thus lowers Vs. For Vp/Vs running between the physically more plausible range of 1.7 to 1.8, the effect on midcrustal Vs is well within stated uncertainties, about  $\pm 9$  m/s.

#### 5.4.4. Vp Radial Anisotropy and $\eta$ in the Crust

[67] As discussed in section 3.1, our inversions are performed with the simplifying but nonphysical assumption that the elastic tensor possesses only Vs anisotropy with  $\gamma = (V_{sh} - V_{sv})/V_s \neq 0$ , but  $V_{ph} = V_{pv}$  so that Vp radial

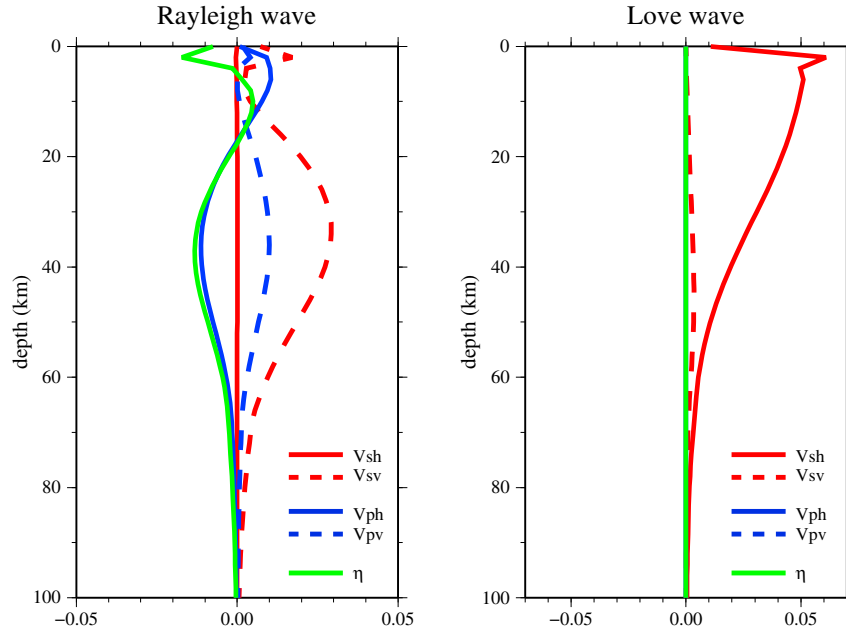


**Figure 18.** Example sensitivity kernels for Rayleigh and Love wave phase speeds at 30 s period to perturbations in  $V_{sv}$ ,  $V_{sh}$ ,  $V_{pv}$ ,  $V_{ph}$ , and  $\eta$  at different depths.

anisotropy  $\varepsilon = (V_{ph} - V_{pv})/V_p = 0$  and  $\eta = 1$ . More realistically, however,  $V_p$  anisotropy is expected to accompany  $V_s$  anisotropy so that  $\varepsilon \neq 0$  and  $\eta \neq 1$ . We discuss the effect of the imposition of this simplification on the posterior distribution of  $V_s$  anisotropy.

[68] Figure 18 presents the sensitivity of Rayleigh and Love wave phase speeds at 30 s period to perturbations in  $V_{sv}$ ,  $V_{sh}$ ,  $V_{pv}$ ,  $V_{ph}$ , and  $\eta$  at different depths. Love waves are sensitive almost exclusively to  $V_{sh}$ , being only weakly sensitive to  $V_{sv}$  and completely insensitive to  $V_{ph}$ ,  $V_{pv}$ , or  $\eta$ . In contrast, Rayleigh waves are sensitive to all of the parameters except  $V_{sh}$ . In order to determine the effect of  $V_p$  anisotropy ( $\varepsilon$ ) and  $\eta$  on our estimate of  $V_s$  anisotropy ( $\gamma$ ), we concentrate on the Rayleigh wave.

[69]  $V_{ph}$  and  $V_{pv}$  have opposite effects on Rayleigh wave phase speeds. Thus, increasing  $V_{ph}$  or decreasing  $V_{pv}$  (i.e., increasing  $\varepsilon$ ) will have a similar effect to decreasing  $V_{sv}$  (Figure 18a). For an isotropic medium, the opposite signs of the  $V_{ph}$  and  $V_{pv}$  kernels cause them to cancel approximately in the deeper parts of the kernel and restrict isotropic  $V_p$  sensitivity to a zone much shallower than primary  $V_s$  sensitivity. But for an anisotropic medium, this is not true. Anisotropic  $V_p$  sensitivity extends as deeply as anisotropic  $V_s$  sensitivity. An increase in  $V_p$  radial anisotropy will decrease the Rayleigh wave phase speed just like an increase in  $V_s$  radial anisotropy. Therefore, as *Anderson and Dziewonski* [1982] point out, the existence of  $V_p$  radial anisotropy will tend to decrease the  $V_s$  radial anisotropy needed to resolve the Rayleigh-Love discrepancy. However, the fifth modulus  $\eta$  must also be taken into account. As shown in Figure 18a, the sensitivity of Rayleigh wave phase speeds to  $\eta$  is similar to that of  $V_{ph}$  so that a decrease in  $\eta$  will increase the Rayleigh wave phase speed, increasing the  $V_s$  radial anisotropy needed to resolve the Rayleigh-Love discrepancy. Thus, an increase (decrease) in  $V_p$  radial anisotropy and a decrease (increase) in  $\eta$  may compensate each other. Whether an

increase in  $V_p$  radial anisotropy is expected to correlate with a reduction in  $\eta$  needs to be explored by investigating the elastic tensor of real crustal rock samples.

[70] For many different crustal and mantle rocks,  $V_p$  radial anisotropy and  $\eta$  can be scaled approximately to  $V_s$  radial anisotropy [*Gung et al.*, 2003; *Becker et al.*, 2008; *Takeo et al.*, 2013]. To obtain approximate scaling relationships, we use the elastic tensors of three crustal rock samples measured by *Erdman et al.* [2013] and provided to us by B. Hacker. Following the procedure described by *Montagner and Anderson* [1989], we rotate the elastic tensors to all possible orientations and compute the five corresponding Love coefficients (A, C, F, L, and N) for every elastic tensor at each orientation. We then analyze the variation of  $V_p$  radial anisotropy ( $\varepsilon$ ) and  $\eta$  as a function of  $V_s$  radial anisotropy ( $\gamma$ ) over all orientations. This analysis shows that the relationship between  $V_p$  and  $V_s$  radial anisotropy is nonlinear, particularly for negative  $V_s$  radial anisotropy ( $\gamma < 0$ ), and  $\varepsilon$  may be nonzero when  $\gamma$  goes to zero. However, ignoring the possible offset between  $\varepsilon$  and  $\gamma$  for weak anisotropy, a linear relationship between  $\gamma$  and  $\varepsilon$  fits the data adequately and we find  $\varepsilon \approx 0.5 \gamma$ . The relationship between  $\eta$  and  $V_s$  radial anisotropy is much more linear with an average slope of about  $-4.2$ , and the offset between  $\eta$  and  $\gamma$  is negligible. As a result, based on the elastic tensor data of *Erdman et al.* [2013], we obtain the following approximate linear scaling relationships between  $V_s$  anisotropy ( $\gamma$ ) with  $V_p$  anisotropy ( $\varepsilon$ ) and  $\eta$ :

$$\varepsilon \approx 0.5 \gamma \quad \eta \approx 1.0 - 4.2 \gamma \quad (5)$$

Thus, an increase in  $V_s$  radial anisotropy is correlated with a smaller increase in  $V_p$  radial anisotropy but a larger decrease in  $\eta$ .

[71] With the scaling relationships summarized in equation (5), we reperform the inversions at four geographical points (A–D of Figure 1a) and present the results in Figure 19. On

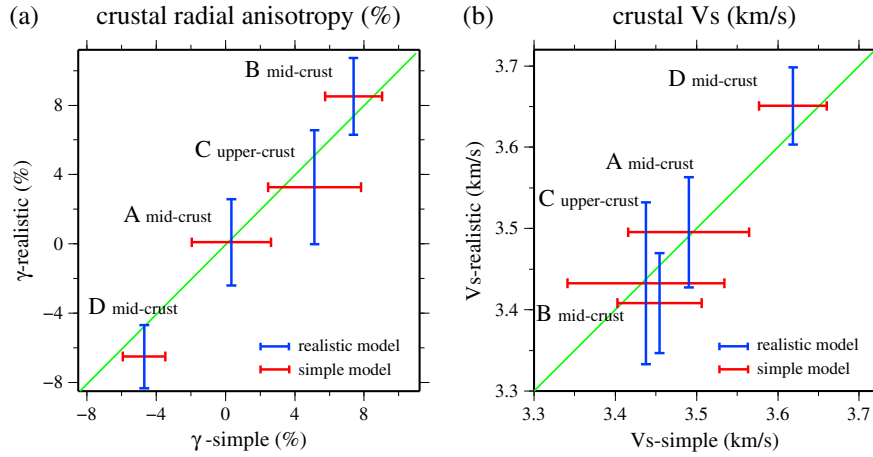


**Figure 19.** Comparison of the inversion results between the simple model of Vs radial anisotropy ( $\gamma$ -simple, red error bars;  $\varepsilon = 0$ ,  $\eta = 1$ ) and the realistic model ( $\gamma$ -realistic, blue error bars;  $\varepsilon = 0.5 \gamma$ ,  $\eta = 1 - 4.2 \gamma$ ) for (a) crustal Vs radial anisotropy and (b) crustal Voigt-averaged Vs. Both plots are for the four locations (A–D) identified in Figure 1a. The results at locations A, B, and D are depth-averaged over the middle crust, while results at location C are depth-averaged over the upper crust. The half-widths of the error bars are the depth-averaged uncertainty ( $1\sigma$ ). Green lines are the locus of points for identical results from the simple and realistic models of Vs radial anisotropy and all error bars overlap this line.

the vertical axis of Figure 19a are the estimates of Vs radial anisotropy ( $\gamma$ ) with the realistic elastic tensor in which Vp anisotropy and  $\eta$  are scaled to Vs anisotropy via equation (5). The horizontal axis presents the estimates of Vs radial anisotropy with the simplified elastic tensor in which all anisotropy is in Vs so that  $\varepsilon = 0$  and  $\eta = 1$ . In each case, the results represent a depth average of Vs anisotropy, which is performed over the upper crust for location C and over the middle crust at the other locations. As expected, the scaling of Vp anisotropy and  $\eta$  to Vs anisotropy has almost no effect at location A where the crust is nearly isotropic, but does have an effect at the locations where there is significant crustal Vs anisotropy. Both the positive (location B) and negative (location D) midcrustal Vs anisotropy tend to increase in amplitude in the inversion based on the more realistic elastic tensor, which means that the amplitude of midcrustal Vs anisotropy presented in section 4 may be slightly underestimated. However, for all four locations, differences between estimates of Vs anisotropy with the simplified or realistic models of radial anisotropy are small, generally lying within the  $1\sigma$  uncertainty because the effects of Vp radial anisotropy and  $\eta$  compensate one another.

#### 5.4.5. Possibility of Overtone Interference?

[72] *Levshin et al.* [2005] discussed how higher modes observed across Central Asia can be used to improve crustal models in this region. The potential existence of higher modes, however, could complicate observations of fundamental mode Rayleigh and Love waves. In the Sichuan Basin, based on our 3-D model, the fundamental and first overtone modes for Love wave should be well separated with a difference between them of at least 350 m/s for periods above 8 s, which is much larger than the observed Rayleigh-Love discrepancy (Figure 7c). Therefore, overtones cannot interfere with fundamental mode Love wave measurements in the Sichuan Basin. However, in Tibet where the crust is much thicker, the fundamental mode and overtone Love waves are closer. Figure 20a presents Love wave group and phase speeds for the fundamental and first overtone modes computed based

on our 3-D model at a point in eastern Tibet (point B of Figure 1a). The group speed of the first Love overtone closely approaches (and can overlap at some locations) the fundamental group speed at about 15 s period. Higher overtones will approach the fundamental mode group speed curves at successive shorter periods. It is, therefore, important to consider if Love wave overtones could be mistaken for the fundamental mode and potentially bias the Love wave phase speed measurements in the period band of our study ( $\geq 8$  s). The relevance of this consideration is amplified by recent observation of *Poli et al.* [2013] of Love wave overtones at periods below about 8 s using ambient noise in the Baltic shield.

[73] In contrast with the observations obtained by *Levshin et al.* [2005] based on intermediate and deep earthquakes in Central Asia, we do not see obvious overtones on FTAN diagrams of ambient noise cross correlations in the region at periods above 6 s. This does not mean that the overtones do not exist because they could be obscured by the fundamental modes. But, the determination of the likelihood of overtone interference reduces to a consideration of the relative excitation of the fundamental and overtone modes. Figure 20b presents theoretical source spectra computed from a horizontal force for the fundamental and first Love overtone modes for source depths of 0 and 20 km (computed at the same location as in Figure 20a). For the surface source, the fundamental mode has much higher amplitude than the first overtone at all periods. However, for a midcrustal source depth, the fundamental and overtone mode have similar amplitudes only below about 8 s period. Figures 20c and 20d illustrate these amplitudes by separately plotting the fundamental and first overtone Green's functions for a horizontal force. Figures 20e and 20f show the FTAN diagrams for these two Green's functions. For the surface source, the overtone does not interfere with measurements of the fundamental mode group or phase speeds across the entire period band of the synthetic seismogram (2–45 s). For the midcrustal source, FTAN picks up the first overtone only at

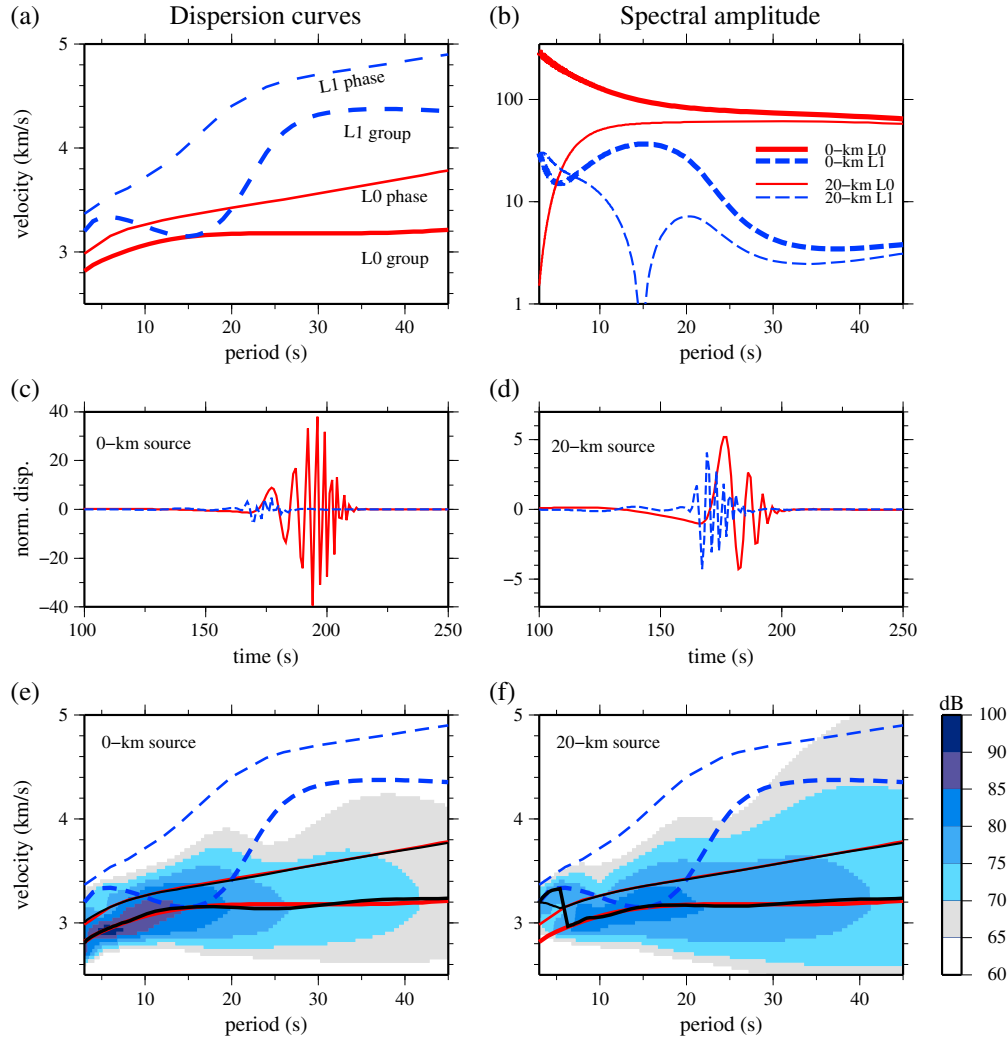


**Figure 20.** Synthetic results for the fundamental and higher mode Love waves. (a) Dispersion curves computed from an isotropic model based on the structure at location B in Figure 1a. Red lines represent phase- and group-velocity dispersion curves of the fundamental model Love wave (L0), and dashed blue lines represent that of the first higher mode Love wave (L1). (b) Spectral amplitudes computed for a horizontal force at the surface (bold lines) or at 20 km depth (thin lines) for the fundamental Love wave (red lines) and first overtone Love wave (dashed blue lines). (c) Green's function computed from the same model in Figure 20a with a single horizontal force located at the surface (0 km depth). Red line indicates the fundamental Love wave; the dashed blue line is the first overtone Love wave. (d) Similar to Figure 20c, but computed with a single horizontal force located at 20 km depth. (e and f) Frequency-time analysis (FTAN) diagram for the superposition of the Green's functions shown in Figures 20c and 20d, respectively. Red and dashed blue lines are the dispersion curves shown in Figure 20a, and black lines are the phase and group velocity dispersion curves measured using FTAN.

periods below  $\sim 6$  s and measures an unbiased fundamental mode at all longer periods. Similar results are found for force couples and double couples.

[74] Although the physical cause of Love waves in ambient noise remains enigmatic, it is likely that they arise from processes near Earth's surface. In this case, the fundamental mode would probably be much stronger than the overtones and overtone interference in measuring fundamental mode Love wave group and phase speeds would probably be minimal at all periods. Even in the unlikely event that ambient noise Love waves were somehow generated at midcrustal depths or there were some other means to deamplify the

fundamental relative to the overtone modes so that the relative amplitude of overtones and fundamental Love waves would be more commensurate, these synthetic results presented here show that the fundamental mode group and phase speeds can be measured accurately at periods above about 6 s.

[75] Rayleigh wave overtones have been observed quite robustly in ambient noise cross correlations in ocean seismograph data [Harmon *et al.*, 2007; Yao *et al.*, 2011] and in basin resonances for waves coming on the continents [Savage *et al.*, 2013] but only at periods below about 5 s and for the basin resonances predominantly on the radial (nonvertical)

component. They are also commonly observed at frequencies above 1 Hz in exploration settings [e.g., *Ritzwoller and Levshin*, 2002]. The period band of these observations does not intersect the current study, and Rayleigh wave overtones are also an unlikely cause of interference with our observations of fundamental mode radial anisotropy.

[76] In conclusion, although the arguments presented here are not definitive, it is highly unlikely that overtones have interfered significantly with the measurement of fundamental mode Love or Rayleigh wave dispersion in the period band of our observations.

#### 5.4.6. Conclusions About Potential Bias in the Posterior Distributions

[77] We have tested how systematic changes to prior information and constraints imposed in the inversion affect the key model attributes that are interpreted in the paper, namely, the amplitude of midcrustal  $V_s$  radial anisotropy and midcrustal Voigt-averaged isotropic  $V_s$ . In particular, we tested the effect of changing the fixed amplitude of radial anisotropy in the upper mantle, the crustal thickness in the reference model, the  $V_p$ : $V_s$  ratio in the crust, and the  $V_p$  radial anisotropy and  $\eta$  in the crust. In general, we find that the midcrustal radial anisotropy will become more positive (i.e.,  $V_{sh}$  will increase relative to  $V_{sv}$ ) by reducing mantle radial anisotropy, increasing crustal thickness, increasing crustal  $V_p$ / $V_s$ , and introducing a more realistic elastic tensor in the crust. Because crustal  $V_p$  radial anisotropy is expected to be anticorrelated with  $\eta$  [*Erdman et al.*, 2013], we show that the introduction of  $V_p$  radial anisotropy with  $\eta$  allowed to differ from unity has the effect of slightly increasing the estimate of midcrustal  $V_s$  radial anisotropy. Similarly, isotropic shear wave speed  $V_s$  also depends to a certain extent on these choices, being inclined to increase with increasing crustal thickness and with decreasing  $V_p$ / $V_s$ . The tests demonstrate, however, that the inference of both positive and negative midcrustal radial anisotropy is robust, and potential bias caused by physically realistic variations in prior information imposed in the inversion should lie within the stated uncertainties of the key model attributes. In addition, we have argued that interference from Love wave (and Rayleigh wave) overtones is expected to affect estimates of crustal  $V_s$  anisotropy negligibly.

[78] Improved constraints on crustal thickness and radial anisotropy in the mantle can be achieved by introducing receiver functions and longer period surface wave dispersion information from earthquake tomography, which are planned for the future.  $V_p$  radial anisotropy and  $\eta$  can be constrained better with improved knowledge of the petrologic composition of the Tibetan crust as more accurate scaling relationships between  $V_s$  anisotropy,  $V_p$  anisotropy, and  $\eta$  are obtained. The observation of higher mode surface waves after earthquakes is another possible direction for improvements in the model. Providing improved constraints on crustal  $V_p$ / $V_s$  may prove to be more challenging, however.

## 6. Discussion

[79] Taking into account the estimated probabilities and the likelihood of bias discussed in section 5, we now address two final questions: What is the most likely cause (or causes) of the radial anisotropy observed beneath and bordering

eastern Tibet? Is there evidence for pervasive partial melt in the middle crust beneath eastern Tibet?

### 6.1. On the Cause of Positive and Negative Radial Anisotropy

[80] Four robust radially anisotropic features are observed. In the middle crust, positive radial anisotropy is observed beneath essentially all of (1) eastern Tibet and (2) the Sichuan Basin and (3) negative anisotropy is found beneath the Longmenshan region bordering eastern Tibet and the Sichuan Basin. (4) In the upper crust, negative radial anisotropy is observed beneath the Songpan-Ganzi terrane and parts of the Qiangtang and Chuandian terranes. We consider the cause of the midcrustal observations first.

[81] Earlier studies [*Shapiro et al.*, 2004; *Huang et al.*, 2010] have interpreted the observation of midcrustal positive radial anisotropy beneath Tibet as evidence for the existence of anisotropic crustal minerals in the middle crust. Recent experimental results, however, have shown that continental crustal minerals such as quartz and feldspars act to dilute the anisotropic response of mica rich rocks [*Ward et al.*, 2012]. This dilution effect may raise doubt into whether crystallographic preferred orientation (CPO) of continental crustal minerals alone can cause strong midcrustal anisotropy. Open or filled fractures [*Leary et al.*, 1990; *Crampin and Chastin*, 2003; *de Figueiredo et al.*, 2013], grain-scale effects [*Hall et al.*, 2008], sedimentary layering [*Valeke et al.*, 2006], other microstructural parameters [*Wendt et al.*, 2003], and sills or lenses of partial melt [*Takeuchi et al.*, 1968; *Kawakatsu et al.*, 2009] have all been discussed as mechanisms to produce seismic anisotropy under certain conditions. Among these mechanisms, partial melt may provide the most viable alternative to CPO to produce midcrustal radial anisotropy. The anisotropic effect of partial melt is less well understood and its ability to produce substantial radial anisotropy is more speculative than CPO. Thus, the observation of crustal radial anisotropy is still best seen as a mapping of the distribution of aligned crustal minerals—albeit with the caveat that the relative fractions of mica, feldspars, quartz, and amphibole remain poorly understood. In the middle crust, we believe that the chief contributor to strong anisotropy is a sheet silicate such as mica (biotite and muscovite).

[82] Even though individual mica crystals exhibit monoclinic symmetry, their tendency to form sheets causes them in aggregate to approximate the much simpler hexagonal symmetry [*Godfrey et al.*, 2000; *Cholach et al.*, 2005; *Cholach and Schmitt*, 2006; *Erdman et al.*, 2013]. There is a unique symmetry axis in a hexagonal system, and we call the plane that is perpendicular to this axis the foliation plane. The amplitude and sign of radial anisotropy reflect the orientation of the symmetry axis (or foliation plane) along with the intrinsic strength of anisotropy, which is determined by mineral content and extent of alignment. The amplitude of azimuthal anisotropy is also affected by the orientation of the symmetry axis [*Levin and Park*, 1997; *Frederiksen and Bostock*, 2000]. Dipping or tilted symmetry axes are believed to be common in many geological settings [*Okaya and McEvilly*, 2003] and should produce a combination of radial and azimuthal anisotropy.

[83] Figure 21 clarifies these expectations by rotating the elastic tensors measured from three crustal rock samples obtained at the Funeral Mountains, the East Humboldt

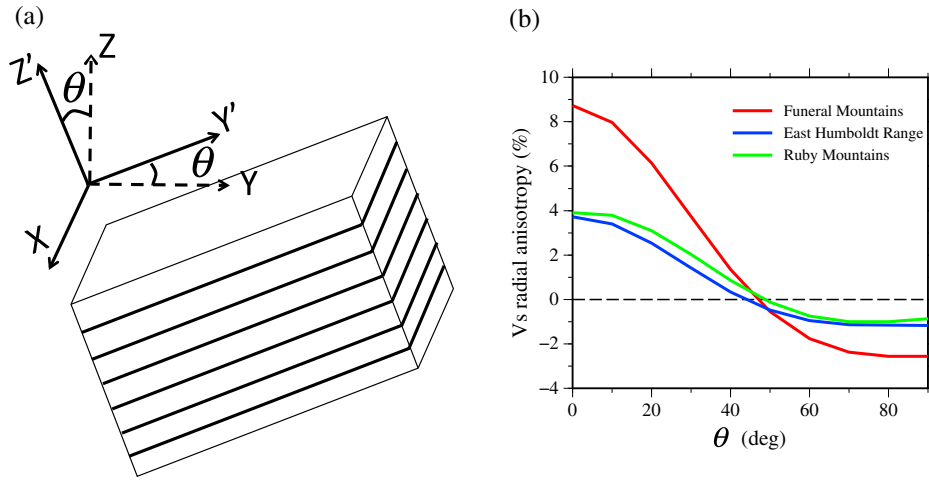


**Figure 21.** (a) Pictorial definition of the rotation angle  $\theta$  for a hexagonally symmetric system. (b)  $V_s$  radial anisotropies,  $\gamma = (V_{sh} - V_{sv})/V_s$ , plotted as a function of rotation angle  $\theta$ , computed by reorientating the elastic tensors of the crustal rock samples of *Erdman et al.* [2013]. Samples locations are identified by line color as indicated.

Range, and the Ruby Mountains by *Erdman et al.* [2013] (and supplied by B. Hacker) through a set of orientations where the symmetry axis ranges from vertical ( $\theta = 0^\circ$ , transverse isotropy) to horizontal ( $\theta = 90^\circ$ ). Similarly, the foliation plane ranges from horizontal to vertical. The result of this calculation is presented in Figure 21b and yields four general conclusions. Radial anisotropy (1) is positive ( $V_{sh} > V_{sv}$ ) and its magnitude maximizes for a vertical symmetry axis ( $\theta = 0^\circ$ ), (2) falls to zero at an intermediate angle  $\sim 50^\circ$ , (3) becomes negative as the symmetry axis exceeds  $\sim 50^\circ$ , and (4) has its maximum negative magnitude between  $60^\circ$  and  $90^\circ$  which is less than the maximum positive magnitude. Therefore, the observed amplitude of radial anisotropy is controlled by a combination of the intrinsic strength of anisotropy, which results from the density of anisotropic minerals and the constructive interference of their effects, and the angle that the symmetry axis makes relative to the local vertical direction. The observation of weaker radial anisotropy alone cannot be interpreted as evidence for a lower density of anisotropic minerals. However, the observation of strong radial anisotropy is evidence for the existence of anisotropic minerals aligned consistently to produce a substantial anisotropic effect. In addition, positive radial anisotropy indicates that the foliation plane is subhorizontal ( $\theta < 10^\circ$ ) to shallowly dipping ( $10^\circ$ – $30^\circ$ ) and negative radial anisotropy implies that it is steeply dipping ( $60^\circ$ – $80^\circ$ ) to subvertical ( $80^\circ$ – $90^\circ$ ). Because the maximum negative amplitude of radial anisotropy is smaller than the maximum positive amplitude, negative anisotropy is a more difficult observation.

[84] Based on these considerations, we conclude that the observations of positive midcrustal radial anisotropy beneath eastern Tibet and beneath the Sichuan Basin imply the existence of planar mica sheets in the middle crust oriented systematically such that the foliation planes are shallowly dipping. We believe that the symmetry axes are not vertical because crustal azimuthal anisotropy is observed across Tibet [e.g., *Yao et al.*, 2010; *Xie et al.*, 2012]. Similarly, the observation of negative midcrustal radial anisotropy along the Longmenshan region is taken as evidence

for planar mica sheets oriented systematically such that the foliation plane is steeply dipping or subvertical. The orientation of the foliation plane (or symmetry axis) cannot be constrained accurately in the absence of information about azimuthal anisotropy, however.

[85] The orientations of the mica sheets in the middle crust probably have dynamical causes. Other than to note that the micas probably orient in response to ductile deformation in the middle crust, we do not speculate on the nature of the deformation that produces this orientation. We do note that the dip angle of faults in the Longmenshan region between Tibet and the Sichuan Basin is high [*Chen and Wilson*, 1996] and that the 2008 Wenchuan earthquake ruptured a steep fault [*Zhang et al.*, 2010]. The change in orientation of the midcrustal foliation plane from shallowly dipping in eastern Tibet to steeply dipping or subvertical in the Longmenshan region may result from the resistance force applied by the rigid lithosphere underlying the Sichuan Basin.

[86] The negative anisotropy observed in the shallow crust ( $\sim 10$  km) across the Songpan-Ganzi terrane and some other parts of eastern Tibet may also result from the CPO of shallower micaceous rocks. However, earthquakes occur to a depth of about 15–20 km within Tibet [*Zhang et al.*, 2010; *Sloan et al.*, 2011], so the crust near 10 km depth where negative anisotropy is observed probably undergoes brittle deformation. Faults and cracks in the upper crust are associated with azimuthal anisotropy [*Sherrington et al.*, 2004] and may also cause radial anisotropy. Negative anisotropy would result from the plane of cracks or faults having a substantial vertical component. We believe this is the most likely source of the observations of negative radial anisotropy in the shallow crust beneath parts of eastern Tibet, particularly the Songpan-Ganzi terrane.

## 6.2. Existence of Pervasive Partial Melt in the Middle Crust Beneath Tibet?

[87] Even under ideal observational circumstances in which  $V_s$  would be exceptionally well constrained, it is difficult to interpret  $V_s$  in terms of the likelihood of partial melt. Consistent with the analysis of *Caldwell et al.* [2009], *Yang*

*et al.* [2012] present a plausibility argument for partial melt setting on below about 3.4 km/s, but this threshold is exceptionally poorly determined and would be expected to vary as a function of crustal composition, wet or dry conditions, and anelastic Q. The average of the means of the posterior distributions of midcrustal shear wave speed taken across eastern Tibet is about  $3.427 \pm 0.050$  km/s. Thus, using the 3.4 km/s threshold value, the mean value of shear wave speed challenges the existence of pervasive midcrustal partial melts across the entirety of eastern Tibet. There are, however, several discrete regions that prefer particularly low midcrustal Vs. Figure 14b identifies the regions in which the inference that  $V_s < 3.4$  km/s is highly probable (or nearly so): the northern Songpan-Ganzi terrane, the northern Chuandian terrane, and part of the central-to-northern Qiangtang terrane. Most of these regions are coincident with high conductance areas from magnetotelluric (MT) studies [Wei *et al.*, 2001; Bai *et al.*, 2010]. The International Deep Profiling of Tibet and the Himalaya (INDEPTH) MT profile [Wei *et al.*, 2001; Unsworth *et al.*, 2004] displays a conductive zone starting at about 25 km depth in the central Qiangtang terrane, and the conductor deepens both northward and southward. In the north Chuandian terrane, Bai *et al.* [2010] also observe a high conductive zone that begins at about 25 km depth.

[88] Therefore, determining with certainty whether Vs lies either above or below 3.4 km/s is difficult using surface wave data alone. But, in summary, there is no compelling evidence that Vs is less than 3.4 km/s pervasively across all of eastern Tibet, although such low shear wave speeds are highly probable in three disjoint regions across the high plateau. Thus, assuming that  $V_s = 3.4$  km/s is an appropriate proxy for the onset of partial melting, we would not expect partial melt to be a pervasive feature of eastern Tibet except in three disjoint regions (the northern Songpan-Ganzi terrane, the northern Chuandian terrane, and part of the central-to-northern Qiangtang terrane) where it should be considered more probable. But this inference is highly uncertain due to the uncertainty of the threshold speed at which partial melt is likely to set on.

## 7. Conclusions

[89] Based on Rayleigh (8 to 65 s period) and Love (8 to 44 s period) wave tomography using seismic ambient noise, we mapped phase velocities across eastern Tibet and surrounding regions using data recorded at PASSCAL and CEArray stations. A Bayesian Monte Carlo inversion method was applied to generate posterior distributions of the 3-D variation of Vsv and Vsh in the crust and uppermost mantle. Summarizing these distributions with their means and standard deviations at each depth and location, we showed that significant midcrustal positive radial anisotropy ( $V_{sh} > V_{sv}$ ) is observed across all of eastern Tibet with a spatially averaged amplitude of  $4.8\% \pm 1.4\%$  and terminates abruptly near the border of the high plateau. Weaker ( $-1.0\% \pm 1.4\%$ ) negative radial anisotropy ( $V_{sh} < V_{sv}$ ) is observed in the shallow crust beneath the Songpan-Ganzi terrane and in the middle crust ( $-2.8\% \pm 0.9\%$ ) near the border of the Tibetan plateau and the Sichuan Basin. Positive midcrustal radial anisotropy ( $5.4\% \pm 1.4\%$ ) is observed

beneath the Sichuan Basin. Shear wave speed in the middle crust is  $3.427 \pm 0.050$  km/s averaged across eastern Tibet.

[90] We also queried the posterior distributions to determine which structural attributes are highly probable and showed the following. (1) Positive midcrustal radial anisotropy is highly probable beneath the eastern high plateau. Lower crustal radial anisotropy is determined more poorly than anisotropy in the middle crust. (2) Isotropic shear wave speeds below 3.4 km/s are possible across most of the high plateau, but are highly probable only beneath the northern Songpan-Ganzi, the northern Chuandian, and part of the Qiangtang terranes. (3) The crustal Vp/Vs ratio is a parameter that is fixed in the inversion, and we set it in the crystalline crust to that of a Poisson solid:  $V_p/V_s = 1.75$ . If a lower (higher) value were chosen, then the amplitude of radial anisotropy would have decreased (increased) and midcrustal Vs would have gone up (down). Vertically averaged crustal Vp/Vs below 1.7 or above 1.8, however, would be hard to justify over large areas of Tibet, and if crustal Vp/Vs ranges between these values, the resulting change to radial anisotropy falls within estimated uncertainties.

[91] A piece of evidence for partial melt in the middle crust would be shear wave speeds at 35 km depth less than about 3.4 km/s [Yang *et al.*, 2012]. Although the maximum likelihood shear wave speed across Tibet at this depth is 3.43 km/s, Vs below 3.4 km/s cannot be formally ruled out particularly if the crystalline crustal Vp/Vs value is above 1.8. Such high values of Vp/Vs are characteristic of mafic mineralogy or partial melt, which are unlikely to extend vertically across the entire Tibetan crust, at least systematically over large areas. Therefore, in light of the uncertainty in the inference of partial melt from shear wave speeds, we do not find incontrovertible evidence for midcrustal partial melt existing pervasively across all of eastern Tibet. However, we do conclude that partial melt is most likely to exist in several discrete regions, notably the northern Songpan-Ganzi, the northern Chuandian, and part of the Qiangtang terranes, where  $V_s < 3.4$  km/s at 35 km depth is highly probable.

[92] We interpret observations of positive midcrustal radial anisotropy beneath eastern Tibet and beneath the Sichuan Basin as evidence for planar mica sheets in the middle crust oriented systematically such that their foliation planes are shallowly dipping ( $10^\circ$ – $30^\circ$  from horizontal) on average. Similarly, the observation of negative midcrustal radial anisotropy in the Longmenshan region along the border separating Tibet from the Sichuan Basin is taken as evidence for planar mica sheets oriented systematically such that their foliation planes are steeply dipping ( $60^\circ$ – $80^\circ$ ) or subvertical ( $80^\circ$ – $90^\circ$ ). We do not speculate on the nature of the deformation that produces this orientation of the mica sheets, but do argue that the change in orientation of the midcrustal foliation plane near the eastern boundary of Tibet from shallowly dipping to steeply dipping or subvertical may result from the resistance force applied by the rigid lithosphere underlying the Sichuan Basin. Finally, the negative anisotropy observed in the shallow crust beneath the Songpan-Ganzi terrane and some other parts of eastern Tibet may be caused by faults and cracks in the upper crust that have a substantial vertical component.

[93] Some of the uncertainty in the estimates of radial anisotropy and in Voigt-averaged shear wave speed Vs results from poor knowledge of the Vp/Vs ratio in the crystalline



crust, of the crustal  $V_p$  radial anisotropy and  $\eta$ , of crustal thickness, and of radial anisotropy in the uppermost mantle. Future improvements in estimates of crustal radial anisotropy and  $V_s$  will depend on developing improved constraints on these structures. Earthquake surface wave tomography would improve knowledge of radial anisotropy in the mantle and in the lowermost crust. Receiver functions can be used to improve constraints on crustal thickness and perhaps also to provide information about the average  $V_p/V_s$  across the crust. Continued improvement in petrologic information about the anisotropy of crustal rocks will provide tighter constraints on the scaling between  $V_p$  radial anisotropy,  $\eta$ , and  $V_s$  radial anisotropy.

[94] **Acknowledgments.** The authors thank two anonymous reviewers and the Associate Editor for insightful comments that helped to improve this paper. They are particularly grateful to Peter Molnar and Anatoli Levshin for advice and support. They also thank Don Anderson, Misha Barmin, Bradley Hacker, David Okaya, and Kevin Mahan for valuable conversations and information as well as the PIs and team members of the PASSCAL experiments, including the Hi-CLIMB, Namche Barwa, MIT-CHINA, Western Tibet, ASCENT/INDEPTH IV experiments, as well as staff members from the PASSCAL Instrument Center for collecting exceptionally valuable data in Tibet. The waveform data from the Chinese stations were provided by the Data Management Centre of the China National Seismic Network at the Institute of Geophysics, China Earthquake Administration. In addition, the facilities of the IRIS Data Management System were used to access some of the data used in this study. The IRIS DMS is funded through the US National Science Foundation under Cooperative Agreement EAR-0552316. This work was supported by US NSF-EAR award 0944022 and also was supported by a Macquarie University Start-up Grant and New Staff Grant to Y. Yang. Aspects of this research also were supported by Chinese Academy of Sciences open grant SKLGED2013-5-1-EZ at the University of Colorado Boulder.

## References

- Acton, C. E., K. Priestley, V. K. Gaur, and S. S. Rai (2010), Group velocity tomography of the Indo-Eurasian collision zone, *J. Geophys. Res.*, *115*, B12335, doi:10.1029/2009JB007021.
- Aki, K., and K. Kaminuma (1963), Phase velocity of Love waves in Japan, 1, Love wave from the Aleutian shock of March 9, 1957, *Bull. Earthquake Res. Inst. Univ. Tokyo*, *41*, 243–260.
- Aki, K. (1964), Study of Love and Rayleigh waves from earthquakes with fault plane solutions or with known faulting Part 2. Application of the phase difference method, *Bull. Seismol. Soc. Am.*, *54*(2), 529–558.
- Anderson, D. L., and A. M. Dziewonski (1982), Upper mantle anisotropy: Evidence from free oscillations, *Geophys. J. R. Astron. Soc.*, *69*, 383–404.
- Babuška, V., and M. Cara (1991), *Seismic Anisotropy in the Earth*, Modern approaches in geophysics, vol. 10, Kluwer Academic Publishers, Dordrecht, The Netherlands, Boston.
- Babuška, V., J.-P. Montagner, J. Plomerová, and N. Girardin (1998), Age-dependent large-scale fabric of the mantle lithosphere as derived from surface-wave velocity anisotropy, *Pure Appl. Geophys.*, *151*(2-4), 257–280, doi:10.1007/s000240050114.
- Bai, D., et al. (2010), Crustal deformation of the eastern Tibetan plateau revealed by magnetotelluric imaging, *Nat. Geosci.*, *3*(5), 358–362, doi:10.1038/ngeo830.
- Barberini, V., L. Burlini, and A. Zappone (2007), Elastic properties, fabric and seismic anisotropy of amphibolites and their contribution to the lower crust reflectivity, *Tectonophysics*, *445*(3–4), 227–244, doi:10.1016/j.tecto.2007.08.017.
- Barmin, M. P., M. H. Ritzwoller, and A. L. Levshin (2001), A fast and reliable method for surface wave tomography, *Pure Appl. Geophys.*, *158*(8), 1351–1375, doi:10.1007/PL00001225.
- Barruol, G., and D. Mainprice (1993), 3-D seismic velocities calculated from lattice-preferred orientation and reflectivity of a lower crustal section: Examples of the Val Sesia section (Ivrea zone, northern Italy), *Geophys. J. Int.*, *115*(3), 1169–1188, doi:10.1111/j.1365-246X.1993.tb01519.x.
- Becker, T., B. Kustowski, and G. Ekström (2008), Radial seismic anisotropy as a constraint for upper mantle rheology, *Earth Planet. Sci. Lett.*, *267*, 213–227.
- Bensen, G. D., M. H. Ritzwoller, M. P. Barmin, A. L. Levshin, F. Lin, M. P. Moschetti, N. M. Shapiro, and Y. Yang (2007), Processing seismic ambient noise data to obtain reliable broad-band surface wave dispersion measurements, *Geophys. J. Int.*, *169*(3), 1239–1260, doi:10.1111/j.1365-246X.2007.03374.x.
- Bensen, G. D., M. H. Ritzwoller, and Y. Yang (2009), A 3-D shear velocity model of the crust and uppermost mantle beneath the United States from ambient seismic noise, *Geophys. J. Int.*, *177*(3), 1177–1196, doi:10.1111/j.1365-246X.2009.04125.x.
- Brocher, T. M. (2005), Empirical relations between elastic wavespeeds and density in the Earth's crust, *Bull. Seismol. Soc. Am.*, *95*(6), 2081–2092, doi:10.1785/0120050077.
- Caldwell, W. B., S. L. Klemperer, S. S. Rai, and J. F. Lawrence (2009), Partial melt in the upper-middle crust of the northwest Himalaya revealed by Rayleigh wave dispersion, *Tectonophysics*, *477*(1–2), 58–65, doi:10.1016/j.tecto.2009.01.013.
- Champion, M. E., N. J. White, S. M. Jones, and K. F. Priestley (2006), Crustal velocity structure in the British Isles: A comparison of receiver functions and wide-angle seismic data, *Geophys. J. Int.*, *166*, 795–813.
- Chen, S. F., and C. J. L. Wilson (1996), Emplacement of the Longmen Shan Thrust–Nappe Belt along the eastern margin of the Tibetan Plateau, *J. Struct. Geol.*, *18*(4), 413–430, doi:10.1016/0191-8141(95)00096-V.
- Chen, Y., J. Badal, and J. Hu (2010), Love and Rayleigh wave tomography of the Qinghai-Tibet Plateau and surrounding areas, *Pure Appl. Geophys.*, *167*(10), 1171–1203, doi:10.1007/s00024-009-0040-1.
- Cholach, P. Y., and D. R. Schmitt (2006), Intrinsic elasticity of a textured transversely isotropic muscovite aggregate: Comparisons to the seismic anisotropy of schists and shales, *J. Geophys. Res.*, *111*, B09410, doi:10.1029/2005JB004158.
- Cholach, P. Y., J. B. Molyneux, and D. R. Schmitt (2005), Flin Flon Belt seismic anisotropy: Elastic symmetry, heterogeneity, and shear-wave splitting, *Can. J. Earth Sci.*, *42*(4), 533–554.
- Christensen, N. I. (1996), Poisson's ratio and crustal seismology, *J. Geophys. Res.*, *101*(B2), 3139–3156, doi:10.1029/95JB03446.
- Christensen, N. I., and W. D. Mooney (1995), Seismic velocity structure and composition of the continental crust: A global view, *J. Geophys. Res.*, *100*(B6), 9761–9788, doi:10.1029/95JB00259.
- Cotte, N., H. Pedersen, M. Campillo, J. Mars, J. F. Ni, R. Kind, E. Sandvol, and W. Zhao (1999), Determination of the crustal structure in southern Tibet by dispersion and amplitude analysis of Rayleigh waves, *Geophys. J. Int.*, *138*(3), 809–819, doi:10.1046/j.1365-246x.1999.00927.x.
- Crampon, S., and S. Chastin (2003), A review of shear wave splitting in the crack-critical crust, *Geophys. J. Int.*, *155*(1), 221–240, doi:10.1046/j.1365-246X.2003.02037.x.
- Duret, F., N. M. Shapiro, Z. Cao, V. Levin, P. Molnar, and S. Roecker (2010), Surface wave dispersion across Tibet: Direct evidence for radial anisotropy in the crust, *Geophys. Res. Lett.*, *37*, L16306, doi:10.1029/2010GL043811.
- Ekström, G., and A. M. Dziewonski (1998), The unique anisotropy of the Pacific upper mantle, *Nature*, *394*(6689), 168–172, doi:10.1038/28148.
- de Figueiredo, J. J. S., J. Schleicher, R. R. Stewart, N. Dayur, B. Omoboya, R. Wiley, and A. William (2013), Shear wave anisotropy from aligned inclusions: Ultrasonic frequency dependence of velocity and attenuation, *Geophys. J. Int.*, *193*, 472–488, doi:10.1093/gji/ggs130.
- Frederiksen, A. W., and M. G. Bostock (2000), Modelling teleseismic waves in dipping anisotropic structures, *Geophys. J. Int.*, *141*(2), 401–412, doi:10.1046/j.1365-246x.2000.00090.x.
- Godfrey, N. J., N. I. Christensen, and D. A. Okaya (2000), Anisotropy of schists: Contribution of crustal anisotropy to active source seismic experiments and shear wave splitting observations, *J. Geophys. Res.*, *105*(B12), 27,991–28,007, doi:10.1029/2000JB900286.
- Gung, Y., M. Panning, and B. Romanowicz (2003), Global anisotropy and the thickness of continents, *Nature*, *422*(6933), 707–711, doi:10.1038/nature01559.
- Guo, Z., X. Gao, H. Yao, J. Li, and W. Wang (2009), Midcrustal low-velocity layer beneath the central Himalaya and southern Tibet revealed by ambient noise array tomography, *Geochem. Geophys. Geosyst.*, *10*, Q05007, doi:10.1029/2009GC002458.
- Hall, S. A., J.-M. Kendall, J. Maddock, and Q. Fisher (2008), Crack density tensor inversion for analysis of changes in rock frame architecture, *Geophys. J. Int.*, *173*(2), 577–592, doi:10.1111/j.1365-246X.2008.03748.x.
- Harmon, N., D. Forsyth, and S. Webb (2007), Using ambient seismic noise to determine short-period phase velocities and shallow shear velocities in young oceanic lithosphere, *Bull. Seismol. Soc. Am.*, *97*(6), 2009–2023, doi:10.1785/0120070050.
- Huang, H., H. Yao, and R. D. van der Hilst (2010), Radial anisotropy in the crust of SE Tibet and SW China from ambient noise interferometry, *Geophys. Res. Lett.*, *37*, L21310, doi:10.1029/2010GL044981.
- James, M., and M. Ritzwoller (1999), Feasibility of truncated perturbation expansions to approximate Rayleigh-wave eigenfrequencies and eigenfunctions in heterogeneous media, *Bull. Seismol. Soc. Am.*, *89*(2), 433–441.
- Jiang, M., A. Galve, A. Hirn, B. de Voogd, M. Laigle, H. P. Su, J. Diaz, J. C. Lepine, and Y. X. Wang (2006), Crustal thickening and variations

- in architecture from the Qaidam basin to the Qang Tang (North-Central Tibetan Plateau) from wide-angle reflection seismology, *Tectonophysics*, 412(3–4), 121–140, doi:10.1016/j.tecto.2005.09.011.
- Jiang, M., S. Zhou, E. Sandvol, X. Chen, X. Liang, Y. J. Chen, and W. Fan (2011), 3-D lithospheric structure beneath southern Tibet from Rayleigh-wave tomography with a 2-D seismic array, *Geophys. J. Int.*, 185(2), 593–608, doi:10.1111/j.1365-246X.2011.04979.x.
- Kanamori, H., and D. L. Anderson (1977), Importance of physical dispersion in surface wave and free oscillation problems: Review, *Rev. Geophys.*, 15(1), 105–112, doi:10.1029/RG015i001p00105.
- Karato, S. (1993), Importance of anelasticity in the interpretation of seismic tomography, *Geophys. Res. Lett.*, 20(15), 1623–1626, doi:10.1029/93GL01767.
- Kawakatsu, H., P. Kumar, Y. Takei, M. Shinohara, T. Kanazawa, E. Araki, and K. Suyehiro (2009), Seismic evidence for sharp lithosphere-asthenosphere boundaries of oceanic plates, *Science*, 324(5926), 499–502, doi:10.1126/science.1169499.
- Kennett, B. L. N., E. R. Engdahl, and R. Buland (1995), Constraints on seismic velocities in the Earth from traveltimes, *Geophys. J. Int.*, 122(1), 108–124, doi:10.1111/j.1365-246X.1995.tb03540.x.
- Kitamura, K. (2006), Constraint of lattice-preferred orientation (LPO) on Vp anisotropy of amphibole-rich rocks, *Geophys. J. Int.*, 165(3), 1058–1065, doi:10.1111/j.1365-246X.2006.02961.x.
- Laske, G., and G. Masters (1997), A global digital map of sediment thickness, *EOS Trans. AGU*, 78, F483.
- Leary, P. C., S. Crampin, and T. V. McEvelly (1990), Seismic fracture anisotropy in the Earth's crust: An overview, *J. Geophys. Res.*, 95(B7), 11,105–11,114, doi:10.1029/JB095B07p11105.
- Levin, V., and J. Park (1997), P-SH conversions in a flat-layered medium with anisotropy of arbitrary orientation, *Geophys. J. Int.*, 131(2), 253–266, doi:10.1111/j.1365-246X.1997.tb01220.x.
- Levshin, A. L., and M. H. Ritzwoller (2001), Automated detection, extraction, and measurement of regional surface waves, *Pure Appl. Geophys.*, 158(8), 1531–1545.
- Levshin, A. L., M. H. Ritzwoller, and L. I. Ratnikova (1994), The nature and cause of polarization anomalies of surface waves crossing northern and central Eurasia, *Geophys. J. Int.*, 117(3), 577–590, doi:10.1111/j.1365-246X.1994.tb02455.x.
- Levshin, A. L., M. H. Ritzwoller, and N. M. Shapiro (2005), The use of crustal higher modes to constrain crustal structure across Central Asia, *Geophys. J. Int.*, 160(3), 961–972, doi:10.1111/j.1365-246X.2005.02535.x.
- Levshin, A. L., X. Yang, M. P. Barmine, and M. H. Ritzwoller (2010), Midperiod Rayleigh wave attenuation model for Asia, *Geochem. Geophys. Geosyst.*, 11, Q08017, doi:10.1029/2010GC003164.
- Li, H., W. Su, C.-Y. Wang, and Z. Huang (2009), Ambient noise Rayleigh wave tomography in western Sichuan and eastern Tibet, *Earth Planet. Sci. Lett.*, 282(1–4), 201–211, doi:10.1016/j.epsl.2009.03.021.
- Lin, F.-C., M. P. Moschetti, and M. H. Ritzwoller (2008), Surface wave tomography of the western United States from ambient seismic noise: Rayleigh and Love wave phase velocity maps, *Geophys. J. Int.*, 173(1), 281–298, doi:10.1111/j.1365-246X.2008.03720.x.
- Lin, F.-C., M. H. Ritzwoller, and R. Snieder (2009), Eikonal tomography: Surface wave tomography by phase front tracking across a regional broadband seismic array, *Geophys. J. Int.*, 177(3), 1091–1110, doi:10.1111/j.1365-246X.2009.04105.x.
- Lin, F. C., M. H. Ritzwoller, Y. Yang, M. P. Moschetti, and M. J. Fouch (2011), Complex and variable crustal and uppermost mantle seismic anisotropy in the western United States, *Nat. Geosci.*, 4(1), 55–61.
- Lloyd, G. E., R. W. H. Butler, M. Casey, and D. Mainprice (2009), Mica, deformation fabrics and the seismic properties of the continental crust, *Earth Planet. Sci. Lett.*, 288(1–2), 320–328, doi:10.1016/j.epsl.2009.09.035.
- Maceira, M., S. R. Taylor, C. J. Ammon, X. Yang, and A. A. Velasco (2005), High-resolution Rayleigh wave slowness tomography of central Asia, *J. Geophys. Res.*, 110, B06304, doi:10.1029/2004JB003429.
- Mahan, K. (2006), Retrograde mica in deep crustal granulites: Implications for crustal seismic anisotropy, *Geophys. Res. Lett.*, 33, L24301, doi:10.1029/2006GL028130.
- Mainprice, D. (2007), Seismic anisotropy of the deep Earth from a mineral and rock physics perspective, in *Treatise in Geophysics*, vol. 2, edited by G. Schubert, pp. 437–492, Elsevier, Oxford, U.K.
- Masters, G., M. P. Barmine, and S. Kientz (2007), Mineos user's manual, in *Computational Infrastructure for Geodynamics*, Calif. Inst. of Technol., Pasadena.
- McEvelly, T. V. (1964), Central U.S. crust—Upper mantle structure from Love and Rayleigh wave phase velocity inversion, *Bull. Seismol. Soc. Am.*, 54(6A), 1997–2015.
- Mechie, J., R. Kind, and J. Saul (2011), The seismological structure of the Tibetan Plateau crust and mantle down to 700 km depth, *Geol. Soc., London, Spec. Publ.*, 353(1), 109–125, doi:10.1144/SP353.7.
- Mechie, J., et al. (2012), Crustal shear (S) velocity and Poisson's ratio structure along the INDEPTH IV profile in northeast Tibet as derived from wide-angle seismic data, *Geophys. J. Int.*, 191(2), 369–384, doi:10.1111/j.1365-246X.2012.05616.x.
- Montagner, J.-P., and H.-C. Nataf (1986), A simple method for inverting the azimuthal anisotropy of surface waves, *J. Geophys. Res.*, 91(B1), 511–520.
- Montagner, J.-P., and D. L. Anderson (1989), Petrological constraints on seismic anisotropy, *Phys. Earth Planet. Inter.*, 54(1–2), 82–105, doi:10.1016/0031-9201(89)90189-1.
- Montagner, J.-P., and T. Tanimoto (1991), Global upper mantle tomography of seismic velocities and anisotropies, *J. Geophys. Res.*, 96(B12), 20,337–20,351, doi:10.1029/91JB01890.
- Moschetti, M. P., and M. H. Ritzwoller, F.-C. Lin, and Y. Yang (2010a), Crustal shear wave velocity structure of the western United States inferred from ambient seismic noise and earthquake data, *J. Geophys. Res.*, 115, B10306, doi:10.1029/2010JB007448.
- Moschetti, M. P., M. H. Ritzwoller, F. Lin, and Y. Yang (2010b), Seismic evidence for widespread western-US deep-crustal deformation caused by extension, *Nature*, 464(7290), 885–889, doi:10.1038/nature08951.
- Nettles, M., and A. M. Dziewoński (2008), Radially anisotropic shear velocity structure of the upper mantle globally and beneath North America, *J. Geophys. Res.*, 113, B02303, doi:10.1029/2006JB004819.
- Nishizawa, O., and T. Yoshino (2001), Seismic velocity anisotropy in mica-rich rocks: An inclusion model, *Geophys. J. Int.*, 145(1), 19–32, doi:10.1111/j.1365-246X.2001.00331.x.
- Okaya, D. A., and T. V. McEvelly (2003), Elastic wave propagation in anisotropic crustal material possessing arbitrary internal tilt, *Geophys. J. Int.*, 153(2), 344–358, doi:10.1046/j.1365-246X.2003.01896.x.
- Okaya, D. A., N. Christensen, D. Stanley, and T. Stern (1995), Crustal anisotropy in the vicinity of the Alpine Fault Zone, South Island, New Zealand, *J. Geol. Geophys.*, 38, 579–583.
- Ozacar, A. A., and G. Zandt (2004), Crustal seismic anisotropy in central Tibet: Implications for deformation style and flow in the crust, *Geophys. Res. Lett.*, 31, L23601, doi:10.1029/2004GL021096.
- Poli, P., H. A. Pedersen, M. Campillo, and the POLENET/LAPNET Working Group (2013), Noise directivity and group velocity tomography in a region with small velocity contrasts: The northern Baltic shield, *Geophys. J. Int.*, 192(1), 413–424, doi:10.1093/gji/ggs034.
- Rapine, R., F. Tilmann, M. West, J. Ni, and A. Rodgers (2003), Crustal structure of northern and southern Tibet from surface wave dispersion analysis, *J. Geophys. Res.*, 108(B2), 2120, doi:10.1029/2001JB000445.
- Readman, P. W., F. Hauser, B. M. O'Reilly, and V. C. Do (2009), Crustal anisotropy in southwest Ireland from analysis of controlled source shear-wave data, *Tectonophysics*, 474, 571–583.
- Ritzwoller, M. H., and A. L. Levshin (2002), Estimating shallow shear velocities with marine multi-component seismic data, *Geophysics*, 67(6), 1991–2004.
- Ritzwoller, M. H., A. L. Levshin, L. I. Ratnikova, and A. A. Egorkin (1998), Intermediate period group velocity maps across Central Asia, Western China, and parts of the Middle East, *Geophys. J. Int.*, 134, 315–328.
- Savage, M. K., F. C. Lin, and J. Towend (2013), Ambient noise cross-correlation observations of fundamental and higher-mode Rayleigh wave propagation governed by basement resonance, *Geophys. Res. Lett.*, 40, 1–6, doi:10.1002/grl.50678.
- Schlue, J. W., and L. Knopoff (1977), Shear wave polarization anisotropy in the Pacific basin, *Geophys. J. R. Astron. Soc.*, 49, 145–165.
- Shapiro, N. M., and M. H. Ritzwoller (2002), Monte-Carlo inversion for a global shear-velocity model of the crust and upper mantle, *Geophys. J. Int.*, 151(1), 88–105, doi:10.1046/j.1365-246X.2002.01742.x.
- Shapiro, N. M., M. H. Ritzwoller, P. Molnar, and V. Levin (2004), Thinning and flow of Tibetan crust constrained by seismic anisotropy, *Science*, 305(5681), 233–236, doi:10.1126/science.1098276.
- Shen, W., M. H. Ritzwoller, and V. Schulte-Pelkum (2013a), A 3-D model of the crust and uppermost mantle beneath the Central and Western US by joint inversion of receiver functions and surface wave dispersion, *J. Geophys. Res. Solid Earth*, 118, 262–276, doi:10.1029/2012JB009602.
- Shen, W., M. H. Ritzwoller, V. Schulte-Pelkum, and F.-C. Lin (2013b), Joint inversion of surface wave dispersion and receiver functions: A Bayesian Monte-Carlo approach, *Geophys. J. Int.*, 192(2), 807–836, doi:10.1093/gji/ggs050.
- Sherrington, H. F., G. Zandt, and A. Frederiksen (2004), Crustal fabric in the Tibetan Plateau based on waveform inversions for seismic anisotropy parameters, *J. Geophys. Res.*, 109, B02312, doi:10.1029/2002JB002345.
- Sloan, R. A., J. A. Jackson, D. McKenzie, and K. Priestley (2011), Earthquake depth distributions in central Asia, and their relations with lithosphere thickness, shortening and extension, *Geophys. J. Int.*, 185(1), 1–29, doi:10.1111/j.1365-246X.2010.04882.x.
- Takeo, A., K. Nishida, T. Isse, H. Kawakatsu, H. Shiobara, H. Sugioka, and T. Kanazawa (2013), Radially anisotropic structure beneath the Shikoku Basin from broadband surface wave analysis of ocean bottom seismometer records, *J. Geophys. Res. Solid Earth*, 118, 2878–2892, doi:10.1002/jgrb.50219.

- Takeuchi, H., Y. Hamano, and Y. Hasegawa (1968), Rayleigh- and Love-wave discrepancy and the existence of magma pockets in the upper mantle, *J. Geophys. Res.*, *73*(10), 3349–3350, doi:10.1029/JB073i010p03349.
- Tatham, D. J., G. E. Lloyd, R. W. H. Butler, and M. Casey (2008), Amphibole and lower crustal seismic properties, *Earth Planet. Sci. Lett.*, *267*(1–2), 118–128, doi:10.1016/j.epsl.2007.11.042.
- Trampert, J., and J. H. Woodhouse (1995), Global phase velocity maps of Love and Rayleigh waves between 40 and 150 seconds, *Geophys. J. Int.*, *122*(2), 675–690, doi:10.1111/j.1365-246X.1995.tb07019.x.
- Unsworth, M., W. Wenbo, A. G. Jones, S. Li, P. Bedrosian, J. Booker, J. Sheng, D. Ming, and T. Handong (2004), Crustal and upper mantle structure of northern Tibet imaged with magnetotelluric data, *J. Geophys. Res.*, *109*, B02403, doi:10.1029/2002JB002305.
- Valcke, S. L. A., M. Casey, G. E. Lloyd, J.-M. Kendall, and Q. J. Fisher (2006), Lattice preferred orientation and seismic anisotropy in sedimentary rocks, *Geophys. J. Int.*, *166*(2), 652–666, doi:10.1111/j.1365-246X.2006.02987.x.
- Vergne, J., G. Wittlinger, Q. Hui, P. Tapponnier, G. Poupinet, J. Mei, G. Herquel, and A. Paul (2002), Seismic evidence for stepwise thickening of the crust across the NE Tibetan plateau, *Earth Planet. Sci. Lett.*, *203*(1), 25–33, doi:10.1016/S0012-821X(02)00853-1.
- Vergne, J., G. Wittlinger, V. Farra, and H. Su (2003), Evidence for upper crustal anisotropy in the Songpan-Ganze (northeastern Tibet) terrane, *Geophys. Res. Lett.*, *30*(11), 1552, doi:10.1029/2002GL016847.
- Villaseñor, A., M. H. Ritzwoller, A. L. Levshin, M. P. Barmin, E. R. Engdahl, W. Spakman, and J. Trampert (2001), Shear velocity structure of central Eurasia from inversion of surface wave velocities, *Phys. Earth Planet. Inter.*, *123*(2–4), 169–184, doi:10.1016/S0031-9201(00)00208-9.
- Wang, C.-Y., L. Zhu, H. Lou, B.-S. Huang, Z. Yao, and X. Luo (2010), Crustal thicknesses and Poisson's ratios in the eastern Tibetan Plateau and their tectonic implications, *J. Geophys. Res.*, *115*, B11301, doi:10.1029/2010JB007527.
- Ward, D., K. Mahan, and V. Schulte-Pelkum (2012), Roles of quartz and mica in seismic anisotropy of mylonites, *Geophys. J. Int.*, *190*(2), 1123–1134, doi:10.1111/j.1365-246X.2012.05528.x.
- Wei, W., et al. (2001), Detection of widespread fluids in the Tibetan crust by magnetotelluric studies, *Science*, *292*(5517), 716–719, doi:10.1126/science.1010580.
- Wendt, A. S., I. O. Bayuk, S. J. Covey-Crump, R. Wirth, and G. E. Lloyd (2003), An experimental and numerical study of the microstructural parameters contributing to the seismic anisotropy of rocks, *J. Geophys. Res.*, *108*(B8), 2365, doi:10.1029/2002JB001915.
- Xie, J., W. Shen, M. H. Ritzwoller, Y. Yang, L. Zhou, Y. Zheng (2012), Imaging crustal anisotropy in eastern Tibet and South China using ambient noise and earthquake data, *AGU fall meeting*, 2012, T33D–2683.
- Xu, L., S. Rondenay, and R. D. van der Hilst (2007a), Structure of the crust beneath the southeastern Tibetan Plateau from teleseismic receiver functions, *Phys. Earth Planet. Inter.*, *165*(3–4), 176–193, doi:10.1016/j.pepi.2007.09.002.
- Xu, Y., Z. Li, and S. W. Roecker (2007b), Uppermost mantle structure and its relation with seismic activity in the central Tian Shan, *Geophys. Res. Lett.*, *34*, L10304, doi:10.1029/2007GL029708.
- Yang, Y., and M. H. Ritzwoller (2008), Characteristics of ambient seismic noise as a source for surface wave tomography, *Geochem. Geophys. Geosyst.*, *9*, Q02008, doi:10.1029/2007GC001814.
- Yang, Y., et al. (2010), Rayleigh wave phase velocity maps of Tibet and the surrounding regions from ambient seismic noise tomography, *Geochem. Geophys. Geosyst.*, *11*, Q08010, doi:10.1029/2010GC003119.
- Yang, Y., M. H. Ritzwoller, Y. Zheng, W. Shen, A. L. Levshin, and Z. Xie (2012), A synoptic view of the distribution and connectivity of the mid-crustal low velocity zone beneath Tibet, *J. Geophys. Res.*, *117*, B04303, doi:10.1029/2011JB008810.
- Yao, H., C. Beghein, and R. D. van der Hilst (2008), Surface-wave array tomography in SE Tibet from ambient seismic noise and two-station analysis - II. Crustal and upper-mantle structure, *Geophys. J. Int.*, *173*, 205–219.
- Yao, H., R. D. van der Hilst, and J.-P. Montagner (2010), Heterogeneity and anisotropy of the lithosphere of SE Tibet from surface wave array tomography, *J. Geophys. Res.*, *115*, B12307, doi:10.1029/2009JB007142.
- Yao, H., P. Gouédard, J. A. Collins, J. J. McGuire, and R. D. van der Hilst (2011), Structure of young East Pacific Rise lithosphere from ambient noise correlation analysis of fundamental- and higher-mode Scholte-Rayleigh waves, *C. R. Geosci.*, *343*(8–9), 571–583, doi:10.1016/j.crte.2011.04.004.
- Yue, H., et al. (2012), Lithospheric and upper mantle structure of the northeastern Tibetan Plateau, *J. Geophys. Res.*, *117*, B05307, doi:10.1029/2011JB008545.
- Zandt, G., and C. J. Ammon (1995), Continental crust composition constrained by measurements of crustal Poisson's ratio, *Nature*, *374*(6518), 152–154, doi:10.1038/374152a0.
- Zhang, Z. M., J. G. Liou, and R. G. Coleman (1984), An outline of the plate tectonics of China, *Geol. Soc. Am. Bull.*, *95*(3), 295–312, doi:10.1130/0016-7606(1984)95<295:AOOTPT>2.0.CO;2.
- Zhang, P., Q. Deng, G. Zhang, J. Ma, W. Gan, W. Min, F. Mao, and Q. Wang (2003), Active tectonic blocks and strong earthquakes in the continent of China, *Sci. China Ser. D-Earth Sci.*, *46*(2), 13–24, doi:10.1360/03dz0002.
- Zhang, P.-Z., X. Wen, Z.-K. Shen, and J. Chen (2010), Oblique, high-angle, listric-reverse faulting and associated development of strain: The Wenchuan Earthquake of May 12, 2008, Sichuan, China, *Annu. Rev. Earth Planet. Sci.*, *38*(1), 353–382, doi:10.1146/annurev-earth-040809-152602.
- Zheng, X.-F., Z.-X. Yao, J.-H. Liang, and J. Zheng (2010), The role played and opportunities provided by IGP DMC of China National Seismic Network in Wenchuan Earthquake disaster relief and researches, *Bull. Seismol. Soc. Am.*, *100*(5B), 2866–2872, doi:10.1785/0120090257.
- Zheng, S., X. Sun, X. Song, Y. Yang, and M. H. Ritzwoller (2008), Surface wave tomography of China from ambient seismic noise correlation, *Geochem. Geophys. Geosyst.*, *9*, Q05020, doi:10.1029/2008GC001981.
- Zhou, L., J. Xie, W. Shen, Y. Zheng, Y. Yang, H. Shi, and M. H. Ritzwoller (2012), The structure of the crust and uppermost mantle beneath South China from ambient noise and earthquake tomography, *Geophys. J. Int.*, *189*(3), 1565–1583, doi:10.1111/j.1365-246X.2012.05423.x.